coatings

MDPI

Review

MXenes in Perovskite Solar Cells: Emerging Applications and Performance Enhancements

Bin Luo [1,†], Xiaodan Wang [2,3,†], Kamale Tuokedaerhan [4], Shuying Wang [4], Chen Wang [1], Xiaohao Shi [1], Zhiqiang Yu [5,*] and Xiangqian Shen [4,6,*]

[1] School of Materials Science and Engineering, Xinjiang University, Urumqi 830046, China; 107552303638@stu.xju.edu.cn (X.S.)
[2] Department Interface Design, Helmholtz-Zentrum Berlin für Materialien und Energie GmbH (HZB), Al-bert-Einstein-Str. 15, 12489 Berlin, Germany
[3] Energy Materials In-Situ Laboratory Berlin (EMIL), HZB, 12489 Berlin, Germany
[4] Xinjiang Key Laboratory of Solid State Physics and Devices, School of Physical Science and Technology, Xinjiang University, Urumqi 830046, China
[5] School of Electronic Engineering, Guangxi University of Science and Technology, Liuzhou 545006, China
[6] State Key Laboratory of Metal Matrix Composites, Shanghai Jiao Tong University, Shanghai 200240, China
* Correspondence: zhiqiangyu@alumni.hust.edu.cn (Z.Y.); sxqlyq@sjtu.edu.cn (X.S.)
† These authors contributed equally to this work.

Abstract: Perovskite solar cells (PSCs) have emerged as promising candidates for next-generation photovoltaic technology due to their remarkable power-conversion efficiencies (PCEs). Since their introduction, the PCE of PSCs has advanced from 3.8% to over 26%. Nonetheless, challenges pertaining to stability and reliability continue to impede their commercial viability. Recent progress in interface engineering and materials science has underscored the potential of two-dimensional (2D) materials, particularly MXenes, in mitigating these challenges. MXenes represent a class of two-dimensional materials with significant potential for application in PSCs, attributed to their exceptional electrical conductivity, high carrier mobility, remarkable optical transparency, chemical stability, and tunable surface chemical properties. When employed as electron transport layers, MXenes enhance charge transfer and extraction efficiency, leading to substantial improvements in PCEs. Furthermore, their integration into hole transport layers and use as interfacial modifiers contribute to the mitigation of degradation pathways, thereby enhancing device longevity. The unique structural and electronic characteristics of MXenes facilitate their application as transparent electrodes, presenting opportunities for cost reduction and improved optical properties. This review provides a comprehensive overview of the current advancements in MXene-based PSCs, emphasizing significant accomplishments and exploring future research directions aimed at enhancing the efficiency and stability of these devices.

Keywords: perovskite solar cells; MXenes; interface engineering; charge transport layer; performance enhancements

Citation: Luo, B.; Wang, X.; Tuokedaerhan, K.; Wang, S.; Wang, C.; Shi, X.; Yu, Z.; Shen, X. MXenes in Perovskite Solar Cells: Emerging Applications and Performance Enhancements. *Coatings* **2024**, *14*, 1564. https://doi.org/10.3390/coatings14121564

Academic Editor: Alessandro Latini

Received: 6 November 2024
Revised: 8 December 2024
Accepted: 11 December 2024
Published: 13 December 2024

1. Introduction

In the continuous quest for sustainable and renewable energy solutions, perovskite solar cells (PSCs) have emerged as strong contenders, distinguished by their remarkable optoelectronic properties, cost-effective fabrication processes, and immense scalability potential [1,2]. In recent years, there has been a significant increase in the power-conversion efficiencies (PCEs) recorded in laboratory settings, rising from an initial 3.8% to over 26%, thereby approaching the theoretical maximum of approximately 31% [1,3–5]. This rapid progression highlights the transformative potential of PSCs in the domain of solar energy conversion. Perovskite crystal structures are generally cubic or octahedral, characterized by the chemical formula ABX_3. Within this structure, the A ions are positioned at the center of

the unit cell and are surrounded by twelve X ions, forming a coordination cuboctahedron with a coordination number of 12. In perovskite materials, typical A-site cations include $CH_3NH_3^+$, FA^+, and Cs^+. The B-site cations are positioned at the vertices of the cubic unit cell and are coordinated by six X-site anions, forming an octahedral geometry with a coordination number of 6. Common B-site anions are Pb^{2+} and Sn^{2+}. The X-sites are typically occupied by halide anions such as I^-, Br^-, or Cl^-. Representative perovskite compounds include $CH_3NH_3PbX_3$, $CsPbI_3$, $CsPbBr_3$, and Cs_4PbI_6 [6]. The distinctive crystal structure of perovskite materials promotes efficient light absorption and charge carrier generation, making them highly promising candidates for solar energy applications [7–11]. This crystal structure of PSCs facilitates the absorption of a broad spectrum of sunlight, enabling the conversion of solar energy into electrical energy with minimal losses, which is crucial for optimizing energy output. Various techniques exist for synthesizing perovskite films, including solution-based methods, vapor deposition techniques, sol-gel processes, and spin-coating approaches. Among these, solution-based methods are particularly advantageous due to their simplicity, cost-effectiveness, and scalability for large-scale production. Nevertheless, achieving uniformity and high crystallinity in the films remains a challenge with this approach. Conversely, the vapor deposition method provides high-quality films and excellent uniformity; however, it is associated with costly equipment, intricate processes, and elevated expenses [12,13].

Despite these advantageous characteristics, the commercialization of PSCs continues to face substantial obstacles, particularly concerning stability and reliability [14–17]. Achieving long-term durability and consistent performance across diverse environmental conditions remains a significant challenge. To address this issue, researchers have extensively explored a wide array of approaches aimed at enhancing device stability and improving overall performance. These strategies include the development of advanced passivation materials to protect the active layer from environmental stressors, the enhancement of grain growth or the implementation of single-crystal technologies to decrease defect density, the optimization of solvent usage to produce more uniform and stable films, the refinement of additives to customize material properties, and the improvement of interface engineering quality to ensure robust electrical connections and minimize energy loss [8–10,18–31].

Among the numerous strategies utilized to attain these objectives, the incorporation of two-dimensional (2D) transition metal carbides and nitrides, referred to as MXenes, has attracted considerable scholarly interest. These materials are characterized by their high electrical conductivity, exceptional carrier mobility, hydrophilic properties, superior optical transparency, chemical stability, and tunable surface chemistry, rendering them highly suitable for diverse applications within PSC architectures [32–45]. Figure 1 illustrates the positions and functions of MXenes. Specifically, their exceptional conductivity and high carrier mobility facilitate efficient charge transfer and extraction within PSC devices, thereby contributing to substantial improvements in PCEs. And MXenes exhibit superior conductivity and tunable surface chemical properties compared to other two-dimensional materials, such as graphene and transition metal sulfides. Additionally, they offer notable advantages in synthesis and processing, allowing them to stand out in a diverse range of materials. Moreover, MXenes' outstanding optical transparency, chemical stability, and adjustable surface chemical properties enable them to play pivotal roles in various PSC components, including electron transport layers (ETLs), hole transport layers (HTLs), interfacial modifiers, and even as transparent electrodes [46–53]. Furthermore, MXenes' chemical stability and resistance to degradation make them ideal for mitigating common degradation pathways in PSCs, thereby extending device longevity [54–57]. Consequently, MXenes are integral to the design of various PSC architectures. In traditional (n-i-p) architectures, MXenes are predominantly utilized as ETLs, capitalizing on their superior conductivity and ability to modulate interfaces to enhance electron extraction and transport. This approach effectively minimizes interfacial defects and reduces non-radiative recombination. Conversely, in inverted (p-i-n) configurations, MXenes are more frequently

employed as HTLs or as materials for interfacial modification. This usage optimizes energy level alignment and interfacial contact, thereby enhancing hole extraction efficiency and improving device stability. These roles collectively contribute to a significant enhancement in overall device performance and long-term reliability of PSCs. The integration of MXenes into PSCs experienced a significant advancement in 2018, marked by the pioneering work of Guo et al. [58]. In their study, $Ti_3C_2T_x$ MXenes were successfully incorporated into the perovskite layer of solar cells. This innovation demonstrated that the inclusion of MXenes could effectively regulate the nucleation process during crystal formation, resulting in the production of larger perovskite grains. Consequently, this led to enhanced performance and efficiency in the solar cells. This seminal discovery has since paved the way for further exploration and application of MXenes within the field of PSC technology.

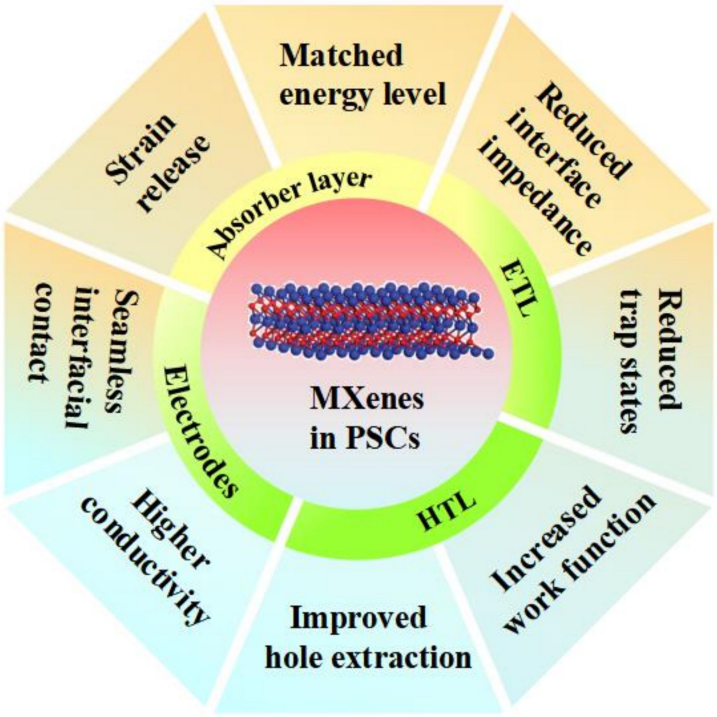

Figure 1. Positions and functions of MXenes in PSCs.

This review seeks to offer an extensive examination of the novel applications and performance improvements of MXenes in PSCs. We will delve into the fundamental properties of MXenes that make them beneficial for PSC applications, analyzing their role in various components of the PSC architecture, such as ETLs, HTLs, and as interfacial modifiers. A critical evaluation of recent advancements will be provided, emphasizing the mechanisms by which MXenes enhance charge separation, transport, and collection, as well as their impact on long-term stability. Additionally, the challenges associated with the synthesis, processing, and scalability of MXene-based PSC components will be discussed, along with potential strategies to overcome these barriers.

2. Synthesis and Properties of MXenes

MXenes represent an innovative class of 2D materials, comprising a family of 2D transition metal carbides, nitrides, and carbonitrides. These materials demonstrate exceptional conductivity, tunable surface properties, and superior mechanical strength. Firstly, MXenes exhibit exceptionally high electrical conductivity, with $Ti_3C_2T_x$ achieving values up to 10,000 S/cm, making them ideal for efficient charge transport layers. Additionally, MXenes demonstrate excellent mechanical strength, with a Young's modulus of approximately 330 GPa, ensuring structural stability and suitability for flexible electronic devices. The typical bandgap of MXenes ranges from 0 to 2 eV, depending on their surface functional

groups (e.g., -OH, -F, and -O), allowing tunable energy levels to adapt to various PSC designs [59,60]. The general chemical formula of MXenes is $M_{n+1}X_nT_x$; in this context, "M" denotes the transition metals (Sc, Ti, Zr, Hf, V, Nb, Ta, Cr, Mo and so on) and "X" represents carbon and/or nitrogen. "T_x" denotes surface terminals, which encompass various modification groups, including -O, -OH, and -F [61,62]. In 2011, Naguib et al. reported for the first time the synthesis of $Ti_3C_2T_x$ MXenes [63]. MXenes represent a novel class of 2D materials characterized by various combinations of M and X elements. These combinations include variations in the number of elements at M and X positions, the number of atomic layers, atomic arrangements, and overall composition. These diverse combinations lead to the formation of surface groups denoted as $\pi(T_x)$, as illustrated in Figure 2 [64].

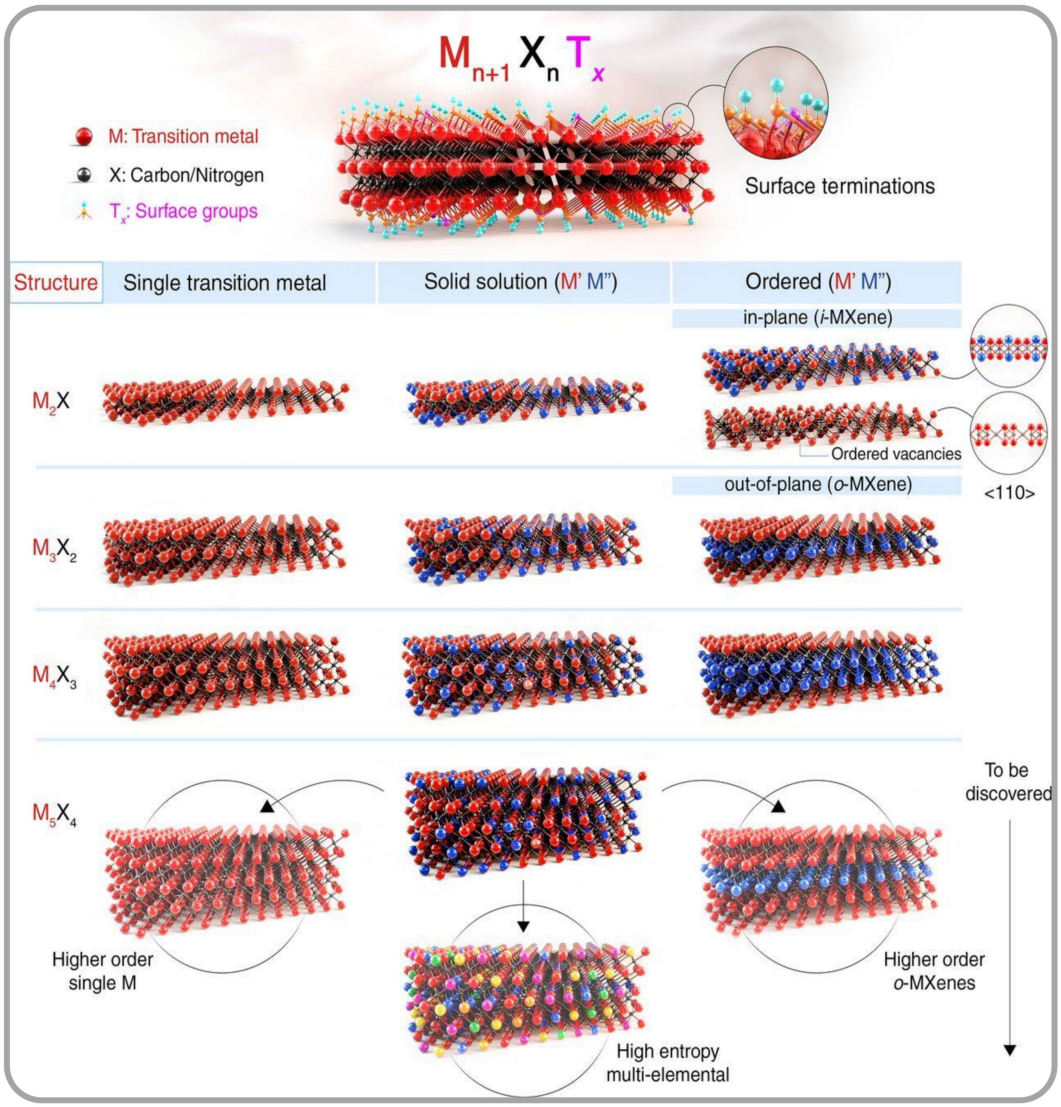

Figure 2. Schematic illustration of the MXene structures. Two-dimensional MXenes have a general formula of $M_{n+1}X_nT_x$, where M is an early transition metal, X is carbon and/or nitrogen, and T_x represents surface terminations of the outer metal layers. The n value in the formula can vary from 1 to 4, depending on the number of transition metal layers (and carbon and/or nitrogen layers) present in the structure of MXenes, for example, Ti_2CT_x (n = 1), $Ti_3C_2T_x$ (n = 2), $Nb_4C_3T_x$ (n = 3), and $(Mo,V)_5C_4T_x$ (n = 4). Reproduction with permission from ref. [64]. Copyright 2021, AAAS.

The synthesis of MXenes typically involves three key steps: preparing a layered precursor, selectively etchingthe A layer (such as aluminum), and exfoliating the structure into single-layer or few-layer MXenes [65–68]. The synthesis of MXenes begins with

the preparation of layered precursors, typically produced through reactive sintering or alternative methods to generate either MAX phase or non-MAX phase layered materials. The chemical composition and structure of these materials greatly affect the performance and properties of MXenes, underscoring the critical nature of this step. In the subsequent step, the A layer must be removed [69]. This process is usually achieved through acid etching or other methods, aimed at removing the A layer from either the MAX phase or non-MAX phase, thus obtaining weakly bonded multilayer MXenes. Finally, the delamination into single or few-layer MXenes is the third step in the synthesis of MXenes, which is typically accomplished through dispersion or other methods [70]. MXenes are generally synthesized by selectively etching A elements (e.g., Al, Ga, Si, or Ge) from the MAX phase, which is classified under groups 13 or 14. Additionally, certain MXenes can be synthesized from non-MAX precursors. The high reactivity of A elements, when compared to M-X bonds, along with the relatively weaker M-A bond strength, facilitates the selective etching of A layers from the MAX phase. This process typically employs either direct hydrofluoric acid (HF) in an aqueous solution or in situ HF generated from a LiF/HCl mixture [60,69,71,72].

Different deposition methods significantly influence the performance of MXenes in PSCs. Common methods include spin coating, spray coating, and vacuum filtration. Among these, spin coating is widely used due to its simplicity and ability to produce uniform films, optimizing charge transport properties. Spray coating and vacuum filtration, on the other hand, are more suitable for large-scale fabrication, balancing performance and cost-effectiveness. The typical thickness range of MXene layers is 5–50 nm, which ensures excellent conductivity while avoiding excessive thickness that could hinder charge transport. For instance, studies have shown that $Ti_3C_2T_x$ films with a thickness of 10–20 nm exhibit optimal charge transport efficiency and interfacial stability, significantly enhancing the power-conversion efficiency and long-term stability of PSCs. The surface chemistry of MXenes can be tailored through various methods to optimize their performance and applications [73]. Common strategies include chemical etching (e.g., using hydrofluoric acid or LiF-HCl) to modify surface terminal groups such as -F, -OH, and =O [74], as well as post-treatments like thermal annealing, chemical modifications (e.g., reactions with organic molecules or metal ions), or electrochemical methods (e.g., oxidation or reduction) to further adjust surface chemistry. These approaches enhance properties like conductivity, hydrophilicity, or catalytic activity.

Current synthesis methods primarily utilize wet acid etching. In recent years, several new synthesis methods have emerged alongside HF-based techniques, including HF combined with other acids, HF with oxidants, $H_2NH_4HF_2$, and HCl with fluoride salts. These new methods encompass Lewis acid salt-assisted etching, alkali treatment under hydrothermal conditions, organic alkali treatment, etching in organic solvents, acoustic synthesis using salt solutions, and electrochemical etching [74–86]. These new methods provide more options and possibilities for the synthesis of MXenes, thereby enhancing research and applications of MXene materials. Although bottom-up approaches have been employed to synthesize MXenes, the majority are produced using top-down methods. This method enables MXenes' structures and compositions to originate from their corresponding bulk layered carbides and nitrides. Bulk transition metal carbides and nitrides display a diverse range of chemical compositions and structures attributed to the stability of metal (M) and non-metal (X) vacancies or mixed occupancy. This diversity endows them with significant potential for applications that range from catalysis to extreme environments. Recently, researchers have focused on historical studies of bulk transition metal carbides and nitrides to regulate the chemical properties of precursors and synthesize MXenes with tunable or extreme properties. By utilizing the chemical diversity found in layered transition metal carbides and nitrides, including MAX and non-MAX phases, researchers have successfully synthesized various MXene compositions. These compositions illustrate MXenes' potential and establish a foundation for their advancement in diverse applications. Moreover, the environmental and economic aspects associated with the synthesis of MXenes are substan-

tial. Conventional synthesis techniques often employ fluoride-containing etchants, such as hydrofluoric acid, alongside strong acids. The utilization and disposal of these substances pose significant environmental pollution risks, thereby escalating remediation expenses. As a result, the advancement of environmentally friendly synthesis methods, such as fluoride-free etching and aqueous phase synthesis, has become a pivotal area of research aimed at reducing environmental hazards. Additionally, MXene synthesis is characterized by its simplicity, scalability, and low production costs, providing considerable economic benefits. However, inadequate waste management during large-scale production could exacerbate the burden of environmental remediation. The multifaceted roles of MXenes as components or additives in PSCs related to passivation defects, crystallinity, electrical conductivity, mechanical flexibility, and moisture resistance will be addressed in the subsequent sections.

3. Application of MXenes in PSCs

3.1. MXenes Applied to Charge Transport Layer

3.1.1. MXenes as Charge Transport Layer

Yang et al. introduced $Ti_3C_2T_x$ MXene nanoflakes as a novel ETL in planar PSCs, subjected to low-temperature processing, and enhanced their performance through UV-ozone treatment. The device structure is depicted in Figure 3a [87]. UV-ozone treatment increases the Ti-O bonds on the surface of $Ti_3C_2T_x$ MXenes, thereby improving electron transport and suppressing recombination. The SEM images of $Ti_3C_2T_x$ films after ultraviolet ozone treatment for different durations are shown in Figure 3(b1–b4). Additionally, the metallic properties of $Ti_3C_2T_x$ MXenes prevent holes from recombining at the interface, further enhancing the performance of the battery. The duration of UV-ozone treatment significantly influences battery performance, with the PCE reaching a maximum of 17.17% after 30 min of treatment [87]. Furthermore, the thickness of the $Ti_3C_2T_x$ MXene layer also impacts the performance of batteries, with thinner layers leading to higher PCE values.

Despite the numerous advantages of 2D $Ti_3C_2T_x$ MXenes, such high transparency, excellent conductivity, tunable work functions, and efficient solution-processing capabilities, the performance of PSCs utilizing MXenes incorporating MXenes remains suboptimal compared to traditional TiO_2 or SnO_2-based solar cells. Several critical interfacial issues between MXenes and perovskites necessitate immediate investigation. Wang et al. synthesized $Ti_3C_2T_x$ MXene films through a room temperature solution process and subsequently improved their surface properties via oxygen plasma treatment [88]. The structural schematic diagram is shown in Figure 3c. Oxygen plasma treatment disrupts certain Ti-C bonds, resulting in the formation of numerous randomly distributed Ti-O bonds. This alteration adjusts the work function of MXenes, reduces trap states, and enhances electronic transport at the interfaces. Characterization techniques, including X-ray photoelectron spectroscopy (XPS) and Raman spectroscopy, confirmed the formation of Ti-O bonds after oxygen plasma treatment. The MXenes treated with oxygen plasma demonstrated excellent optoelectronic performance as an ETL in PSCs. The top-performing devices achieved a PCE of 18.9%, one of the highest levels reported for MXenes-based PSCs to date. As shown in Figure 3d,e, the MXenes-based devices treated with oxygen plasma exhibited enhanced stability in ambient air, retaining approximately 80% of their initial PCE over 750 h. In contrast, untreated MXenes devices showed a decline in efficiency to 10% within 700 h [88].

Furthermore, several research teams have achieved significant advancements in the application of MXenes in the ETL layer. Qian et al. applied $Ti_3C_2T_x$ films onto indium tin oxide (ITO) substrates via the spin-coating method and subsequently conducted UV-ozone treatment to enhance their effectiveness as ETLs [89]. The $Ti_3C_2T_x$ MXenes, utilized as the ETL, achieved a PCE of 22.77%. This improvement in efficiency is primarily due to the exceptional electrical conductivity of MXenes and their effectiveness in facilitating charge transfer. Under ambient conditions with humidity levels between 40% and 60%, the battery maintained a stability of 95% after 1000 h of testing. This finding indicates that MXenes not only enhance battery efficiency but also improve tolerance under humid conditions. The incorporation of MXenes significantly enhances the charge transfer charac-

teristics of the battery. As an ETL, $Ti_3C_2T_x$ MXenes effectively facilitate electron extraction and transport, thus minimizing charge recombination losses. Furthermore, optimizing the interface between MXenes and the perovskite layer leads to enhancements in PCE and reductions in non-radiative recombination losses. Adjusting the work function of MXenes via chemical synthesis methods allows for improved energy level alignment [90]. Additionally, the incorporation of MXenes reduces the defect density within the perovskite layer. Nb_2C MXenes, when used as an additive in the SnO_2 ETL, significantly enhance the surface energy and crystal quality of SnO_2, which in turn improves the quality of the perovskite film and its charge transport properties [91]. Zhao et al. demonstrated that MXene-H doped SnO_2 displays improved band alignment characteristics, as evidenced by density functional theory (DFT) calculations and ultraviolet photoelectron spectroscopy (UPS) measurements [92]. Furthermore, functionalized MXene nanosheets exhibit high electrical conductivity and mobility. This property allows them to form zero Schottky barrier heterojunctions with SnO_2, which effectively enhances carrier transport and improves moisture resistance and photostability. Moreover, incorporating functionalized MXene can enhance the grain size of perovskite films by modulating the surface energy. This adjustment results in a notable increase in PCE from 20.98% in undoped films to 23.66%. The optimal device attains a PCE of 24.12% and an FF exceeding 0.84. Zhang et al. utilized amino-functionalized niobium carbide MXene as the ETL and as an additive in methylammonium-free PSCs [93]. Replacing the surface fluorine (-F) groups with amino ($-NH_2$) groups reduced the work function of MXene from 4.65 eV to 4.32 eV, aligning it with the lowest conduction band edge of the perovskite layer. This modification enhanced electron transport efficiency and significantly improved the PCE of the device, achieving a maximum of 21.79%. Additionally, the unencapsulated devices retained 93% of their initial PCE after 1500 h of storage, indicating good stability.

In PSCs, the HTL is essential for both the crystallization of the perovskite film and the efficiency of hole transfer at the perovskite/HTL interface. Organic hole transport materials, such as N,N′-bis(3-methylphenyl)-N,N′-bis(phenyl), although theoretically outstanding, are limited in large-scale practical applications due to the complexity of their synthesis and purification processes, as well as their high costs [94–96]. In contrast, while common inorganic materials like nickel oxide (NiO_x) demonstrate good performance, their processing temperatures exceed 200 °C, thereby limiting their use in flexible devices. Within this context, niobium carbide MXenes (Nb_2CT_x) exhibit significant potential as a novel type of hole transport material (HTM) [97,98]. They demonstrate superior electrical properties and can be tailored for various applications by modifying their work function (WF). In comparison to other multilayer MXenes, Nb_2CT_x comprises only three atomic layers and features a larger specific surface area, enhancing its interaction with the perovskite layer and consequently improving the charge transfer capability. The work function of Nb_2CTx can be modified by altering the types and quantities of surface groups, thus offering flexibility in its practical applications [99].

Zhang et al. reported that the initial work function of Nb_2CT_x was approximately 4.68 eV, which was insufficient to support efficient hole transport. However, after treatment with oxygen plasma, the work function increased to 5.04 eV, benefiting from the increase in surface oxygen groups [100]. During processing, oxygen atoms withdraw electrons from niobium atoms, leading to a reduction in Fermi level, an elevation in vacuum level, and subsequent increases in the work function. This modification reduces energy loss at the interface between the HTL and the perovskite absorption layer, thereby promoting effective hole transfer, minimizing charge recombination, and ultimately improving the J_{SC}. As a result, PSCs utilizing oxygen plasma-treated Nb_2CT_x achieved a maximum PCE of 20.74%. Furthermore, these devices demonstrated PCEs of 17.26% and 17.94% in flexible and large-area (0.99 cm^2) devices, indicating significant improvements compared to untreated Nb_2CT_x-based PSCs (18.1%) and those without an HTL (15.5%) [100]. Notably, the oxygen plasma-treated PSCs exhibited excellent flexibility and long-term stability,

sustaining optimal performance even under high-temperature conditions of up to 85 °C. The structural schematic diagram and the J-V curve of PVSC are shown in Figure 4a,b.

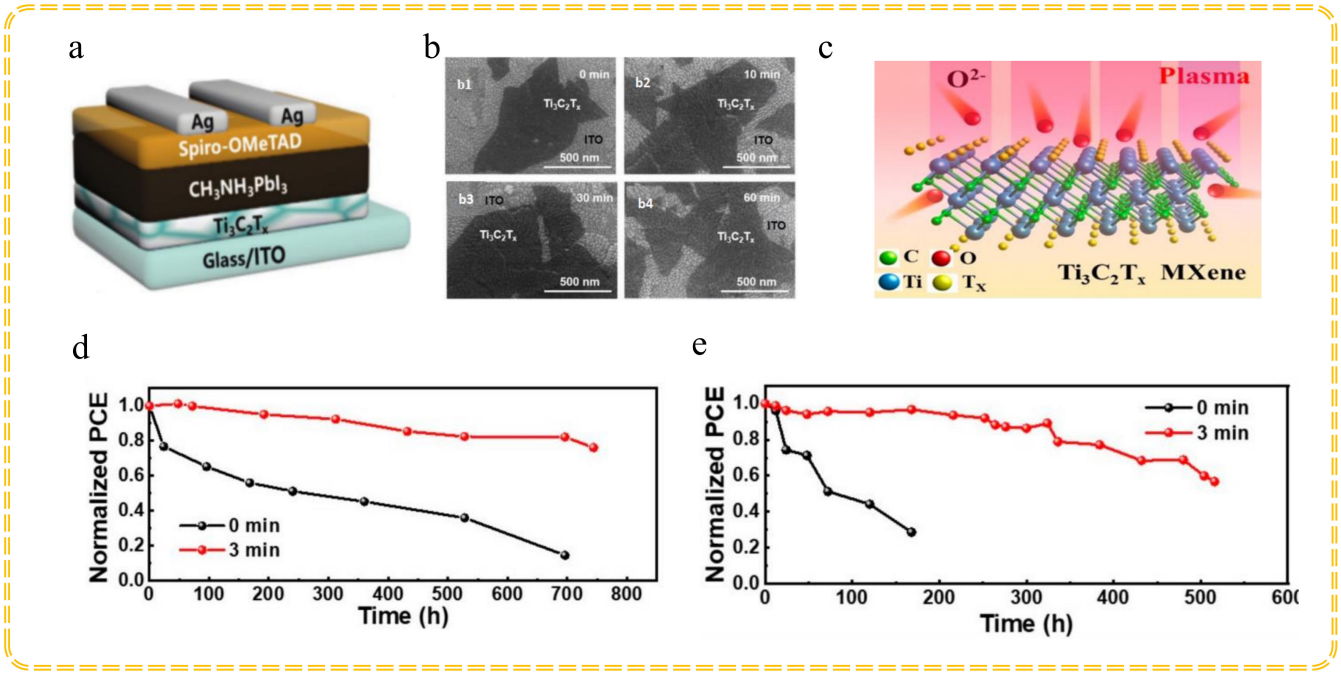

Figure 3. (**a**) Device architecture of ITO/ETL/$CH_3NH_3PbI_3$/Spiro-OMeTAD/Ag based on $Ti_3C_2T_x$ with/without UV-ozone treatment as ETL; (**b1**–**b4**) SEM images of the original $Ti_3C_2T_x$ film and $Ti_3C_2T_x$ films treated with UV ozone for 10, 30, and 60 min, respectively. Reproduction with permission from ref. [87]. Copyright 2019, Wiley; (**c**) schematic diagram of $Ti_3C_2T_x$ MXenes structure treated with oxygen plasma; for the photostability test, the solar cells were irradiated by the 100 mW cm^{-2} white LED continuously in atmosphere without encapsulation. (**d**) Storage stability and (**e**) photostability tests of PSCs in ambient air (relative humidity ~50%) without encapsulation. Reproduction with permission from ref. [88]. Copyright 2021, American Chemical Society.

Despite the significant improvements in the PCE of PSCs, challenges such as stability, production scalability, and high-temperature processing persist. To address these issues, exploring new materials and methods to enhance performance and manufacturability remains crucial. Wang et al. investigated the effects of incorporating different concentrations of SCA into $Ti_3C_2T_x$ MXenes via spray coating technology on the film quality and photoelectric performance [101]. The structural schematic diagram is shown in Figure 4c. As shown in Figure 4d, their findings revealed that adding 0.3 V/V% SCA significantly improved the coverage and uniformity of $Ti_3C_2T_x$ films. The SCA-treated $Ti_3C_2T_x$ optimized the hole transport pathways, improved hole extraction efficiency, and decreased transport resistance at the interface between the HTL and the perovskite. As a result, the HTL of the PSC with this material improved the PCE from 11.12% to 13.65%. The J-V curve of PSCs is shown in Figure 4e. Moreover, the $Ti_3C_2T_x$-based PSC incorporating the SCA additive exhibited enhanced stability under ambient humidity and room temperature conditions, retaining approximately 80% of its initial PCE after 80 h [101].

3.1.2. MXenes as Additives in the Charge Transport Layer

Zhong et al. discovered that by optimizing the ratio of $Ti_3C_2T_x$ to SnO_2 (0–2.2 wt%), the mixed ETL could significantly reduce the defect density in the perovskite films, from 5.65×10^{15} cm^{-3} to 2.25×10^{15} cm^{-3} [102]. After employing the optimized mixed ETL consisting of 1.4 wt% $Ti_3C_2T_x$, a notable increase in short-circuit current density (J_{SC}) and fill factor (FF) was observed, leading to a rise in PCE of PSCs from 16.28% to 20.35%. Furthermore, the incorporation of MXenes resulted in increased grain size of the perovskite

films, decreased surface roughness, and improved optical absorption. The application of the mixed ETL significantly enhanced the environmental stability of unencapsulated devices. Under ambient conditions of 25 °C and 30% relative humidity, devices incorporating the mixed ETL retained approximately 74% of their initial efficiency after 768 h, compared to 41% for devices with pure SnO_2 ETL. Zhong et al. suggested that surface functional groups of MXenes, such as -F and -OH, likely interact with organic cations in the perovskite, facilitating nucleation and growth processes. This interaction improves the quality and performance of the films [102]. The structural schematic diagram, correlation graphs between average particle size/rms surface roughness and MXene content, J-V curves, etc., are shown in Figure 5a–c.

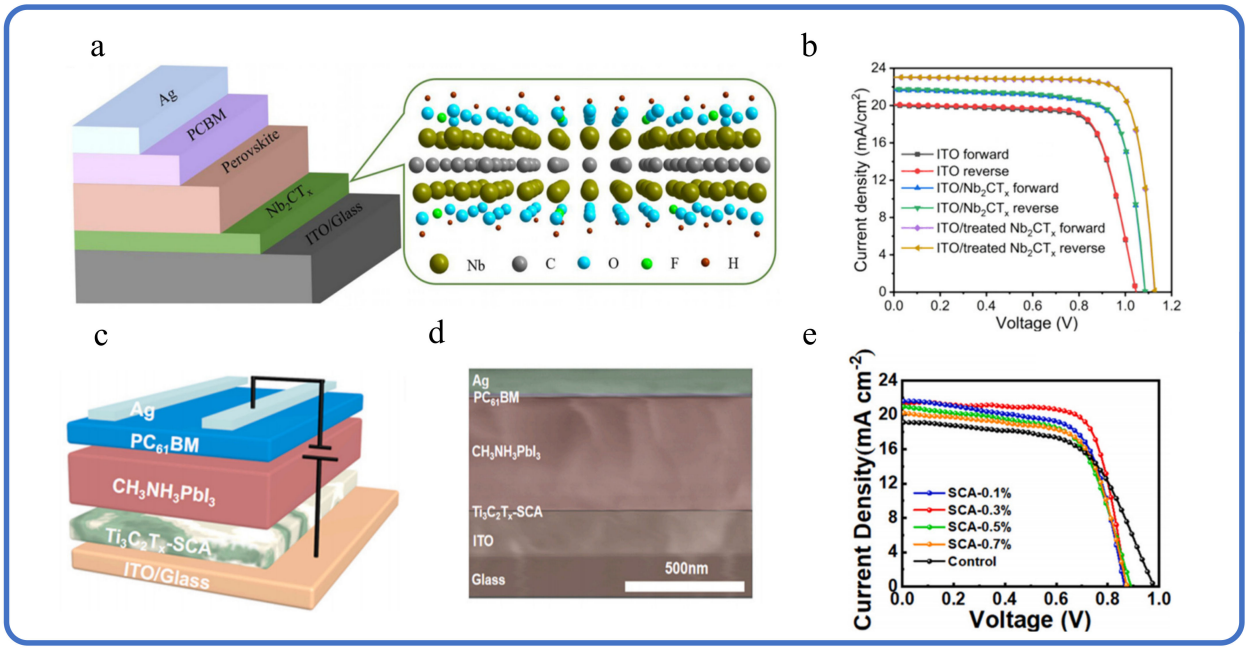

Figure 4. (**a**) The schematic diagram of device structure and the structure of Nb_2CT_x MXenes; (**b**) J-V curves of PVSCs measured under different scan directions. Reproduction with permission from ref. [100]. Copyright 2021, Applied Physics Letters; (**c**) schematic diagram of a device with ITO/HTL/perovskite/$PC_{61}BM$/Ag structure. (**d**) SEM cross-sectional image of $Ti_3C_2T_x$-0.3% HTL device. (**e**) The J-V curve of PSCs is based on $Ti_3C_2T_x$, with different volume fractions of SCA as HTL. Reproduction with permission from ref. [101]. Copyright 2021, Elsevier.

Although organic–inorganic hybrid perovskite materials, such as methylammonium lead iodide (MAPI), perform exceptionally well in photovoltaic applications, their PCE is still below the thermodynamic limit. The primary cause of this limitation is the defects found in the perovskite thin films and their interfaces, which result in charge recombination losses. To address these challenges, Chava et al. proposed reducing recombination losses by optimizing the interface structure and achieving better energy level alignment between the perovskite and the charge transport layer (CTL). The schematic diagram of its planar structure and the energy level diagram are shown in Figure 5d,e. They incorporated MXenes into $PC_{61}BM$ to create M-$PC_{61}BM$ ETL, resulting in a significant increase in the PCE of the cells from 15.2% to 18% [103]. This enhancement primarily results from the n-type doping effect of MXenes, leading to improved conductivity and energy level alignment of $PC_{61}BM$. However, when MXenes are used solely as the ETL, battery performance declines significantly, with a PCE of only 1.6%. This suggests that the energy level alignment of MXenes is not conducive to efficient electron transport. When used as an interface layer, MXenes enhance the energy level alignment between $PC_{61}BM$ and the perovskite layer. This improvement reduces interfacial recombination losses and further increases both the open-circuit voltage (V_{OC}) and FF. Furthermore, the surface groups of MXenes

effectively passivate defects in the perovskite, mitigate non-radiative recombination, and extend carrier lifetime. Current-voltage (I–V) measurements reveal that the conductivity of M-$PC_{61}BM$ is significantly greater than that of undoped $PC_{61}BM$, providing further evidence of its superior performance in batteries.

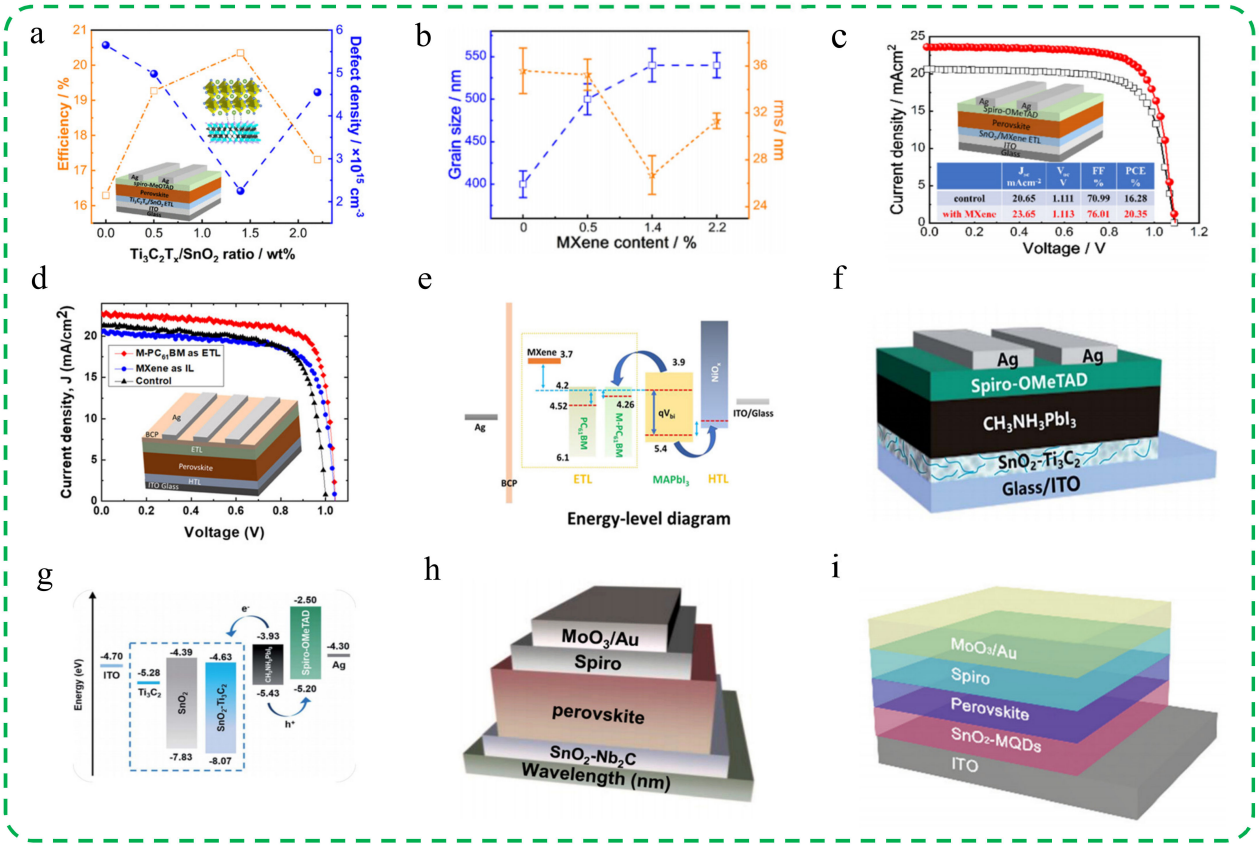

Figure 5. (**a**) Schematic diagram of PSC and MXenes with perovskite, efficiency, and defect density values with respect to -$Ti_3C_2T_x/SnO_2$ wt%; (**b**) correlation plots between average grain size/rms surface roughness and the MXene contents; (**c**) J-V curves. Reproduction with permission from ref. [102]. Copyright 2021, American Chemical Society; (**d**) schematic of a cross-sectional view of a planar p-i-n PSC device and current density; (**e**) energy-level band diagram. Reproduction with permission from ref. [103]. Copyright 2021, American Chemical Society; (**f**) device architecture of ITO/ETL/$CH_3NH_3PbI_3$/Spiro-OMeTAD/Ag based on representative SnO_2–Ti_3C_2 as the ETL; (**g**) schematic energy-level diagram of each layer. Reproduction with permission from ref. [104]. Copyright 2019, The Royal Society of Chemistry; (**h**) schematic of the PSCs structure used in this study. Reproduction with permission from ref. [91]. Copyright 2021, Elsevier; (**i**) schematic of the planar heterojunction structure used for the SnO2-based PSCs. Reproduction with permission from ref. [105]. Copyright 2021, The Royal Society of Chemistry.

The PCE of perovskite materials has significantly increased from 3.8% to over 23%. Despite this advancement, these materials continue to face several challenges, including limited electron extraction capability, poor environmental stability, and insufficient low-temperature processability. Traditional ETL materials, such as TiO_2, require high-temperature sintering, which restricts their application in large-area, flexible, or wearable devices. In contrast, SnO_2 has emerged as a widely utilized ETL material due to its superior electron mobility, favorable optical transparency, and capability for low-temperature processing. Yang et al. synthesized SnO_2-Ti_3C_2 nanocomposites by combining Ti_3C_2 MXenes with SnO_2 at varying compositions (0, 0.5, 1.0, 2.0, and 2.5 wt%) to serve as ETL in low-temperature processed planar structure PSCs [104]. The schematic diagram of its planar structure and the energy level diagram are shown in Figure 5f,g. Adding 1.0 wt%

Ti_3C_2 to SnO_2 increased the PCE of the battery from 17.23% to 18.34%. In comparison, the use of pure Ti_3C_2 as the ETL resulted in a PCE of only 5.28%. Furthermore, the incorporation of Ti_3C_2 enhanced the interfacial properties between the SnO_2 ETL and the perovskite layer, facilitating improved charge transport pathways, reducing charge recombination, and enhancing charge transfer efficiency. The V_{OC} and FF of the battery were also enhanced. Electrochemical impedance spectroscopy (EIS) analysis demonstrated that Ti_3C_2 significantly reduced the interfacial charge transfer resistance (R_rec). With the SnO_2 ETL containing 1.0 wt% Ti_3C_2, both V_{OC} and FF achieved their optimal values. Ultimately, the SnO_2-Ti_3C_2-based PSC demonstrated good environmental stability, retaining approximately 80% of its initial PCE after 768 h of testing [104].

To identify new materials that enhance the performance of ETL and improve the efficiency and stability of PSC, Niu et al. first introduced Nb_2C MXenes as an external additive to the SnO_2 ETL, as shown in Figure 5h. They prepared SnO_2-Nb_2C composites by mixing Nb_2C MXenes with SnO_2 [91]. The analysis using high-angle annular dark field scanning transmission electron microscopy (HAADF-STEM) demonstrates that incorporating Nb_2C MXenes significantly increases the grain size of SnO_2. Additionally, the increase in lattice spacing enhances the roughness and surface energy of SnO_2. This structural optimization facilitates the deposition of perovskite films, leading to higher-quality films with enhanced crystallinity and improved charge carrier transport capabilities. Furthermore, the effect of Nb_2C MXenes on interfacial charge transfer resistance indicates that they can effectively suppress charge recombination, thereby improving the V_{OC} and FF of the battery. In performance tests, the PSC utilizing a SnO_2-Nb_2C ETL achieved a maximum PCE of 22.86%. This represents a significant improvement over the control device without Nb_2C, which had a PCE of 18.96% [91]. Furthermore, after testing in an environment of 25 °C and 40–60% humidity for 40 days, these batteries maintained 98% of their initial efficiency, demonstrating good long-term stability.

The bottom interface is critical in the preparation of perovskite films, influencing the crystallization of the perovskite layer. High crystallinity and low defect density are essential for the performance of PSCs. Nevertheless, comprehensive studies on the crystallization dynamics of perovskite layers influenced by SnO_2 ETLs remain insufficient. Employing synchrotron-based 2D grazing incidence X-ray diffraction (2D-GIXRD) technology, Yang et al. conducted an initial investigation into the crystallization dynamics of perovskite layers modulated by SnO_2 ETL, as shown in Figure 5h. This study elucidated the progression from nucleation to the intermediate phase, ultimately culminating in the perovskite phase [105]. Yang et al. modified the SnO_2 ETL using modified titanium carbide ($Ti_3C_2T_x$) MXene quantum dots (MQDs), resulting in the formation of the MQDs-SnO_2 ETL. The MQDs-SnO_2 ETL significantly accelerates the nucleation process of perovskite, facilitates the formation of intermediate perovskite phases from the precursor solution, and enhances the crystal quality and phase stability of perovskite thin films. Additionally, the superior charge extraction properties of the MQDs-SnO_2 ETL facilitate the efficient transfer of electrons from the perovskite layer to the SnO_2 layer. This results in a steady-state photovoltaic conversion efficiency of up to 23.3% and impressive stability under humidity and illumination. The integral J_{SC} value of 24.39 mA·cm^{-2} closely aligns with the observed J_{SC} value of 24.96 mA·cm^{-2} recorded using a solar simulator [105].

As previously noted, besides the complex synthesis and purification processes, various factors adversely affect performance. These include the poor conductivity of inorganic hole transport materials (e.g., Cu_2CuOx, Fe_2O_3, CuSCN, and Cu_2NiOx), low carrier mobility, inadequate resistance to processing solvents, and low transmittance in the ultraviolet-visible spectrum. Wang et al. explored the use of hematite (α-Fe_2O_3) as an alternative to traditional titanium dioxide (TiO_2) in planar heterojunction PSCs [106]. The SEM images of the FTO substrate are shown in Figure 6a,b. Compared to TiO_2 ETLs, α-iron(III) oxide (α-Fe_2O_3)-based solar cells exhibit minimal performance degradation after 30 days of storage in ambient air, indicating superior stability. Nevertheless, challenges such as inadequate conductivity, interface compatibility, light-absorption efficiency, process complexity, and

long-term stability must be addressed promptly. Hideyuki Tanaka and his research team utilized doped poly(3-hexylthiophene-2,5-diyl) (P3HT) as the HTL in organic–inorganic hybrid solar cells [107]. The structural schematic diagram is shown in Figure 6c. Research indicates that coating a properly doped P3HT onto a 99.5% non-porous perovskite active layer increases the PCE of solar cells from 9.2% to 12.4%. Additionally, issues related to temperature stability, light stability, charge mobility, interface compatibility, preparation complexity, and material costs restrict the commercial application of this material as a hole transport layer in PSCs. Liu et al. employed graphene oxide (GO) as the HTL in PSCs due to its excellent solubility, adjustable energy levels, and cost-effectiveness [108]. The schematic diagram of its planar structure and the energy level diagram are shown in Figure 6d,e. By optimizing the thickness and surface functionalization of GO, the researchers attained efficient and stable PSCs, achieving a maximum PCE of 4.37%. The work function of GO aligns with materials such as P3HT, thereby facilitating efficient charge extraction. Although the conductivity of GO can be enhanced through functionalization and post-treatment, its intrinsic conductivity is still lower than that of some traditional materials, such as PEDOT:PSS. Additionally, the insulating properties of GO lead to increased series resistance at certain thicknesses, consequently reducing the FF and PCE of the solar cells.

Over the past decade, while there has been some advancement in enhancing PCE, the overall performance of bulk heterojunction (BHJ) solar cells remains constrained by factors including inadequate light absorption, suboptimal nanomorphologies, and low charge carrier mobility of the active layer materials. Consequently, researchers have investigated the incorporation of carbon nanotubes (CNTs) into organic BHJ solar cells to augment their performance. As shown in Figure 6f, Yu et al. attained a notable enhancement in PCE, achieving 8.6%, through the incorporation of nitrogen-doped multi-walled carbon nanotubes (N-MCNTs) into the polymer blend of PTB7 and fullerene acceptor $PC_{71}BM$ within BHJ solar cells [109]. The unique structure and conductive properties of N-MCNTs facilitate the formation of an efficient charge transport pathway within the active layer, enhancing both charge separation and carrier mobility. Incorporating N-MCNTs increases the nanocrystal size, thereby providing additional interfaces for light absorption and enhancing light flux capture capability. Furthermore, N-MCNTs affect the phase separation within the nanostructure by reducing the domain size between PTB7 and $PC_{71}BM$. Optimizing the phase separation structure significantly enhances the recombination of electrons and holes, resulting in improved exciton dissociation and migration efficiency. N-MCNTs promote rapid charge transport and minimize chances of charge recombination. This effect enhances both the J_{SC} and the FF, ultimately leading to a significant increase in PCE. Moreover, through careful structural optimization, N-MCNTs achieve a more uniform dispersion within the active layer, thereby enhancing the overall stability and efficiency of the battery materials [109].

Traditional HTL materials, such as PEDOT:PSS, exhibit good conductivity and transparency; however, they suffer from acidity and hygroscopicity, which can negatively impact the long-term performance of devices. Consequently, researchers are exploring the combination of novel materials, such as MXenes, with PEDOT:PSS to enhance the charge transport characteristics and interfacial stability of HTLs. Jongwan Jung and colleagues incorporated N-MCNTs and molybdenum disulfide (Mo_2C) as additives into HTLs for PSCs [110]. Research demonstrates that the composite material created by combining Mo_2C and CNTs with PEDOT:PSS significantly increases the PCE of solar cells, achieving a value of 11.98%. This indicates a significant enhancement compared to pure PEDOT:PSS (9.17%), Mo_2C@PEDOT:PSS (9.82%), and CNT@PEDOT:PSS (10.61%). The incorporation of Mo_2C not only enhances charge transport properties but also decreases the internal resistance of the cell, subsequently improving charge extraction and transport efficiency. Additionally, the Mo_2C-CNT composite material exhibits strong performance in X-ray Diffraction (XRD), achieving a maximum sensitivity of 3.56 $mA/Gy{\cdot}cm^2$ [110]. The struc-

tural schematic diagram, cross-sectional FESEM images, and ITO energy level diagram are shown in Figure 6g–i.

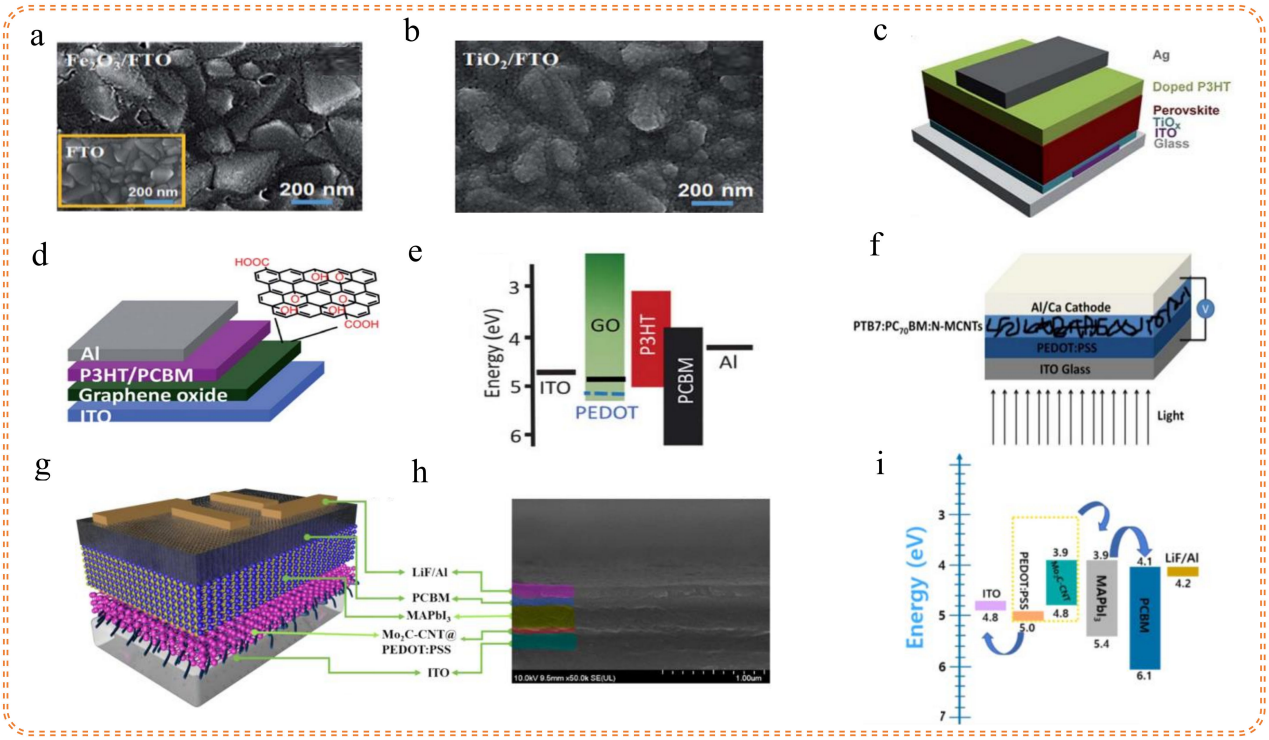

Figure 6. Top view SEM images of the (**a**) α-Fe_2O_3/FTO thin film and (**b**) TiO_2/FTO thin film. Inset of (**a**) shows the typical surface morphology of the FTO substrate. Reproduction with permission from ref. [106]. Copyright 2016, The Royal Society of Chemistry; (**c**) illustration of the present solar cell architecture. Reproduction with permission from ref. [107]. Copyright 2014, The Royal Society of Chemistry; (**d**) schematic illustration of the PSC device structure with GO as the HEL; (**e**) energy level diagrams of the bottom electrode ITO, interlayer materials (PEDOT:PSS, GO), P3HT (donor), and PCBM (acceptor), and the top electrode Al. Reproduction with permission from ref. [108]. Copyright 2014, The Royal Society of Chemistry; (**f**) schematic of device structures used in this work. Reproduction with permission from ref. [109]. Copyright 2013, American Chemical Society; (**g**) device architecture of prepared ITO/HTL/$CH_3NH_3PbI_3$/PCBM/LiF/Al prototype using Mo_2C-CNTs@PEDOT:PSS HTL and (**h**) cross-sectional FESEM image; (**i**) energy level diagram for ITO/Mo_2C-CNTs@PEDOT:PSS/$CH_3NH_3PbI_3$/PCBM/LiF/Al structure. Reproduction with permission from ref. [110]. Copyright 2021, Elsevier.

Because of their excellent electrical conductivity and the presence of surface hydroxyl groups, MXenes are regarded as optimal modifiers for PEDOT:PSS aqueous solutions. Building on this knowledge, Jongwan Jung and his team explored the application of additional materials. They functionalized WO_3 nanoparticles onto 2D conductive $Ti_3C_2T_x$ MXene sheets, resulting in a MXene/WO_3 composite structure that was integrated with PEDOT:PSS to function as the HTL in PSCs [111]. The high conductivity and superior interfacial contact of the composite materials enhance charge transport and extraction, thereby reducing charge recombination. The PSC incorporating an MXene/WO_3/PEDOT:PSS HTL achieves a PCE of 12.26%, significantly exceeding that of HTLs composed solely of WO_3 or MXene. The MXene/WO_3 composite material optimizes the interface between the HTL and the perovskite active layer, enhancing charge transfer and collection capabilities and improving energy level alignment, which facilitates charge extraction and absorption. Furthermore, the high hydrophobicity of MXenes enhances contact on the HTL surface, further increasing hole transport efficiency and decreasing charge recombination processes, thereby improving the long-term stability of the device. The MXene/WO_3 composite HTL

has also been utilized in XRD, demonstrating a high sensitivity of 3.67 mA Gy^{-1} cm^{-2}, highlighting its potential for detection applications [111].

Their dual functionality as both ETL and HTL arises from their unique properties. Firstly, MXenes' high conductivity (e.g., $Ti_3C_2T_x$ with electrical conductivity up to ~10,000 S/cm) and low work function (~4.1 eV) enable efficient electron extraction and transport, making them ideal for ETL applications. Furthermore, through surface functionalization (e.g., introducing -OH or -F groups), the work function of MXenes can be tuned to higher values (~5.0 eV), achieving energy level alignment with hole transport layers, thus making them suitable as HTLs. Experimental results indicate that photovoltaic devices utilizing MXenes as both ETL and HTL exhibit superior charge separation and transport efficiency, with PCE values exceeding 23.34% [40]. This dual functionality not only simplifies device architecture but also reduces fabrication costs, offering a novel approach for designing efficient and cost-effective optoelectronic devices.

MXenes exhibit excellent electrical conductivity, with values reaching 10^3–10^4 S/cm, which is significantly higher than that of TiO_2 (~10^{-5} S/cm) and doped Spiro-OMeTAD (~10^{-3} S/cm). This high conductivity substantially reduces the interfacial resistance of the charge transport layer, thereby enhancing charge extraction efficiency and improving the device's power conversion efficiency (PCE) [112]. Moreover, the surface chemical properties of MXenes can be tailored through surface groups (such as -OH, -F, -O), allowing for better interfacial contact with the perovskite layer, reducing interfacial defect density and suppressing non-radiative recombination. For instance, studies have reported that after incorporating MXenes (such as $Ti_3C_2T_x$) into the electron transport layer, the PCE of the device increased from 18.7% to 21.6%, while utilizing MXenes in the hole transport layer resulted in a PCE of up to 22.7%, significantly outperforming traditional TiO_2 and Spiro-OMeTAD [113,114].

In terms of stability, MXenes demonstrate higher chemical stability and environmental adaptability. TiO_2, as an electron transport layer, is prone to generate oxygen vacancies due to photo-excitation, leading to increased interfacial defects and performance degradation, whereas Spiro-OMeTAD demonstrates poor stability in humid and thermal environments due to reliance on dopants (such as Li-TFSI) [2]. In contrast, the layered structure and surface groups of MXenes can effectively protect their performance from environmental impacts. For example, perovskite solar cells based on MXenes retained over 90% of their initial efficiency after continuous operation at 85 °C for 500 h, whereas the efficiency of traditional materials typically declines to below 70% [115].

In addition to the MXene materials discussed in the figure above used in PSCs, we also provide a comprehensive list in Table 1, which includes a range of recently utilized MXene materials in the ETL and HTL in PSC literature.

Table 1. The role of MXenes as charge transport layer/additive in PSC charge transport layer.

Device Structure	J_{SC} (mA/cm^2)	V_{OC} (V)	FF (%)	PCE (%)	Refs
ITO/$Ti_3C_2T_x$-UV-30 min/$CH_3NH_3PbI_3$/Spiro-OMeTAD/Ag	22.63	1.080	70.00	17.17	[87]
ITO/$Ti_3C_2T_x$/$CH_3NH_3PbI_3$/Spiro-OMeTAD/Au	21.5	0.880	90.00	18.90	[88]
ITO/SnO_2-Nb_2C/$CH_3NH_3PbI_3$/Spiro-OMeTAD/Ag	25.29	1.138	79.50	22.86	[91]
ITO/$Ti_3C_2T_x$-H-doped SnO_2/$FAPbI_3$/Spiro-OMeTAD/MoO_x/Ag	25.49	1.121	84.42	24.12	[92]
TO/T-Nb_2CT_x/$FA_{0.85}Cs_{0.15}PbI_3$ + T-Nb_2CT_x/Spiro-OMeTAD/Ag	25.07	1.124	77.36	21.79	[93]
ITO/Nb_2CT_x/$MAPbI_3$/PCBM/Ag	22.75	1.172	79.80	20.74	[100]
ITO/$Ti_3C_2T_x$-0.3%/Perovskite/$PC_{61}BM$/Ag	21.30	-	73.47	13.65	[101]
ITO/SnO_2/$Ti_3C_2T_x$/$CH_3NH_3PbI_3$/Spiro-OMeTAD/Ag	23.65	1.113	76.00	20.35	[102]
ITO/NiO_x/MAPI/M-$PC_{61}BM$/BCP/Ag	22.75	1.040	76.00	17.95	[103]
ITO/SnO_2/$CH_3NH_3PbI_3$/Spiro-OMeTAD/Ag	22.83	1.050	72.00	17.23	[104]
ITO/SnO_2/MQDs-SnO_2/$CH_3NH_3PbI_3$/Spiro-OMeTAD/Ag	24.96	1.172	79.80	23.34	[105]
ITO/SnO_2/$FA_{0.9}MA_{0.05}Cs_{0.05}PbI_{0.98}Br_{0.02}$/Spiro-MeOTAD/$MoO_3$/Au (C)	24.26	1.140	75.80	20.96	
ITO/TiO_x/Perovskite/P3HT (H-3)/Ag	19.10	0.980	66.30	12.40	[107]
PTB7:$PC_{71}BM$:1.5 wt% N-MCNTs	17.76	0.710	69.00	8.60	[109]
Mo_2C-CNT@PEDOT:PSS	22.78	0.860	61.00	11.98	[110]
MXene/WO_3@PEDOT:PSS	22.47	0.906	60.02	12.26	[111]

3.2. MXenes as Additives in Perovskite Absorber Layers

Despite the significant advancements in photovoltaic conversion efficiency achieved by organic–inorganic hybrid PSCs, there remain substantial opportunities for further enhancement. Researchers have identified crystal size in perovskite thin films as a critical factor influencing performance. Consequently, additive engineering to improve crystal growth and charge transport has become a major research focus. The layered structure and adjustable surface chemical properties of MXenes significantly influence the crystal growth of perovskite thin films [116,117]. The crystal quality of perovskite films is a key determinant of their optoelectronic properties. Additionally, incorporating MXenes facilitates the growth of larger crystals while reducing the number of grain boundaries. In 2018, Ma et al. published the first report on using MXenes in PSCs, incorporating $Ti_3C_2T_x$ MXenes into the $CH_3NH_3PbI_3$ ($MAPbI_3$) perovskite absorption layer, as shown in Figure 7a,b. The addition of $Ti_3C_2T_x$ effectively enhances both the crystal growth and charge transfer properties of the perovskite film [58]. The termination groups of $Ti_3C_2T_x$ effectively slow the crystallization rate of perovskites, leading to the formation of larger crystals, which reduces grain boundaries and enhances the mobility of charge carriers. The research team optimized the additive concentration and found that 0.03 wt% $Ti_3C_2T_x$ improved device performance by 12%. Consequently, the PCE of the PSCs improved from 15.54% to 17.41% [58].

To enhance the performance of PSCs processed via low-temperature solutions, Yasuhiro Shirai and colleagues developed a novel surface passivation technique using an amine polymer, PFN-P1, as an additive in the perovskite layer. As shown in Figure 7c–f, this method improves both the crystallization quality of the perovskite film and the overall efficiency of the solar cells [118]. PFN-P1 acts as a surfactant, promoting uniform crystallization, reducing size variation among perovskite crystals, and mitigating charge extraction inefficiencies at the interfaces. Researchers incorporated PFN-P1 into the perovskite film via a spin-coating process, successfully achieving films with uniform grain distribution. This approach significantly enhanced the open-circuit voltage and PCE, achieving a maximum efficiency of 13.2% with a standard deviation of only 0.40, demonstrating excellent reproducibility. Time-of-flight secondary ion mass spectrometry (TOF-SIMS) analysis revealed that the addition of PFN-P1 improved the surface morphology of the perovskite film and effectively suppressed charge recombination, leading to increased open-circuit voltage and FF of the device. Furthermore, devices incorporating PFN-P1 retained approximately 90% of their initial efficiency for over six months, underscoring its advantages in long-term stability [118].

Sang Hyuk Im et al. applied surface engineering techniques on the $CsPbI_3$ perovskite layer through a spray coating method, which significantly enhanced both the efficiency and stability of the device, as shown in Figure 7g,h [119]. The incorporation of OMXenes provides a physical barrier against moisture intrusion and enhances the electric field at the interface between the perovskite and the ETL, thereby improving charge separation. The research team created an OMXenes-$CsPbI_3$ composite surface layer by combining OMXenes nanosheets with $CsPbI_3$ precursors. This composite layer allows the perovskite layer to maintain good stability under humid, high-temperature, and illuminated conditions. Experimental results indicate that PSCs treated with OMXenes attained a PCE of 19.69% for an area of 0.096 cm^2, while a minimum module of 25 cm^2 achieved an efficiency of 14.64%. Additionally, the encapsulated minimum module preserved approximately 85% of its initial efficiency after 1000 h of light exposure at 85 °C and 85% relative humidity [119].

Doping MXenes can both regulate the energy level alignment between the perovskite absorption layer and the electron transport layer, and effectively passivate the trap states within the battery structure. This process enhances the efficiency of charge extraction and collection. Antonio Agresti et al. investigated the role of MXenes in inverted PSCs based on nickel oxide (NiO) [114]. As shown in Figure 8a, integrating $Ti_3C_2T_x$ MXenes into the perovskite and PCBM (phenyl-C_{61}-butyric acid methyl ester) layers increased the PCE of the battery to over 19%. The MXene-doped batteries demonstrated significant

enhancements in J_{SC} and FF, and they outperformed the reference devices regarding stable power output [114]. Agresti et al. focused on the study of $Ti_3C_2T_x$ MXenes. As shown in Figure 8b, the researchers incorporated $Ti_3C_2T_x$ nanosheets into the perovskite precursor solution, successfully fabricating 2D Ruddlesden–Popper perovskite films. This process resulted in an increase in PCE from 13.69% to 15.71% [120]. At the same time, the incorporation of $Ti_3C_2T_x$ nanosheets facilitated the uniform formation of the perovskite film, reducing grain boundaries and defects, which accelerated the vertical charge transport process. XRD analysis indicated that the crystal quality of the perovskite film significantly improved following the incorporation of $Ti_3C_2T_x$. Additionally, the growth direction of the film became more oriented perpendicular to the substrate, which further enhanced charge transport efficiency. As shown in Figure 8c, Moreover, the presence of $Ti_3C_2T_x$ effectively reduced the trap state density in the perovskite film, thereby improving the optoelectronic performance of the solar cell. Regarding stability, the unencapsulated $Ti_3C_2T_x$-doped solar cells demonstrated excellent performance in an environment with a relative humidity of 55 ± 5%, retaining 80% of the initial PCE after 750 h, while the control group cells only maintained 40% of their PCE after 700 h [120].

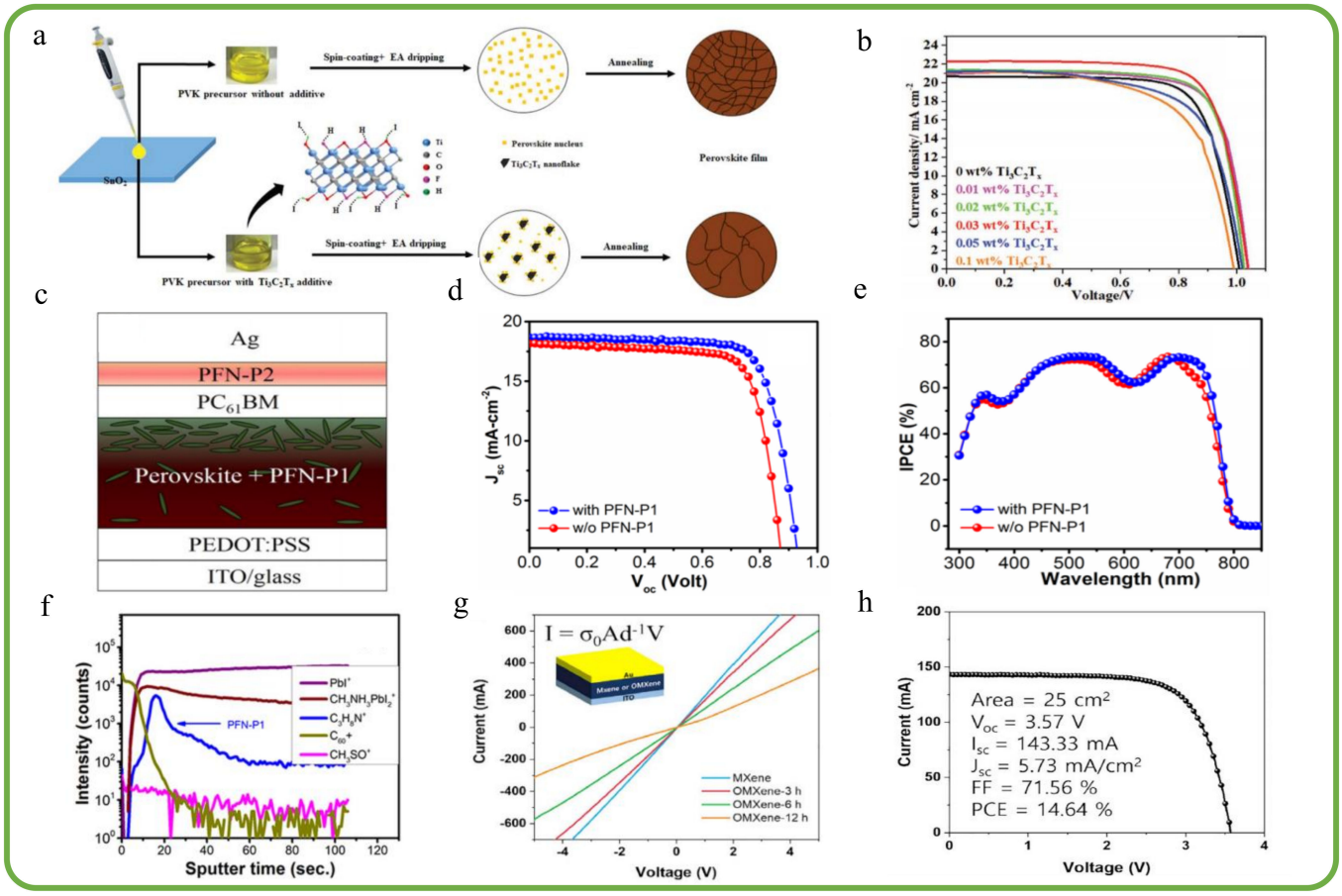

Figure 7. (**a**) Proposed nucleation and growth route of perovskite film with and without $Ti_3C_2T_x$ additive. (**b**) J-V curves of PSCs with different amounts of $Ti_3C_2T_x$. Reproduction with permission from ref. [58]. Copyright 2018, Wiley; (**c**) schematic of device configuration; (**d**) J-V characteristics; (**e**) IPCE spectra of devices with and without PFN-P1; (**f**) TOF-SIMS depth profiles of ITO/PEDOT:PSS/perovskite/PFN-P1/PCBM. Reproduction with permission from ref. [118]. Copyright 2016, American Chemical Society; (**g**) current-voltage characteristics of the ITO/MXene or OMXene/Au devices; (**h**) I–V curve of a $CsPbI_3$ perovskite minimodule. Reproduction with permission from ref. [119]. Copyright 2022, ScienceDirect.

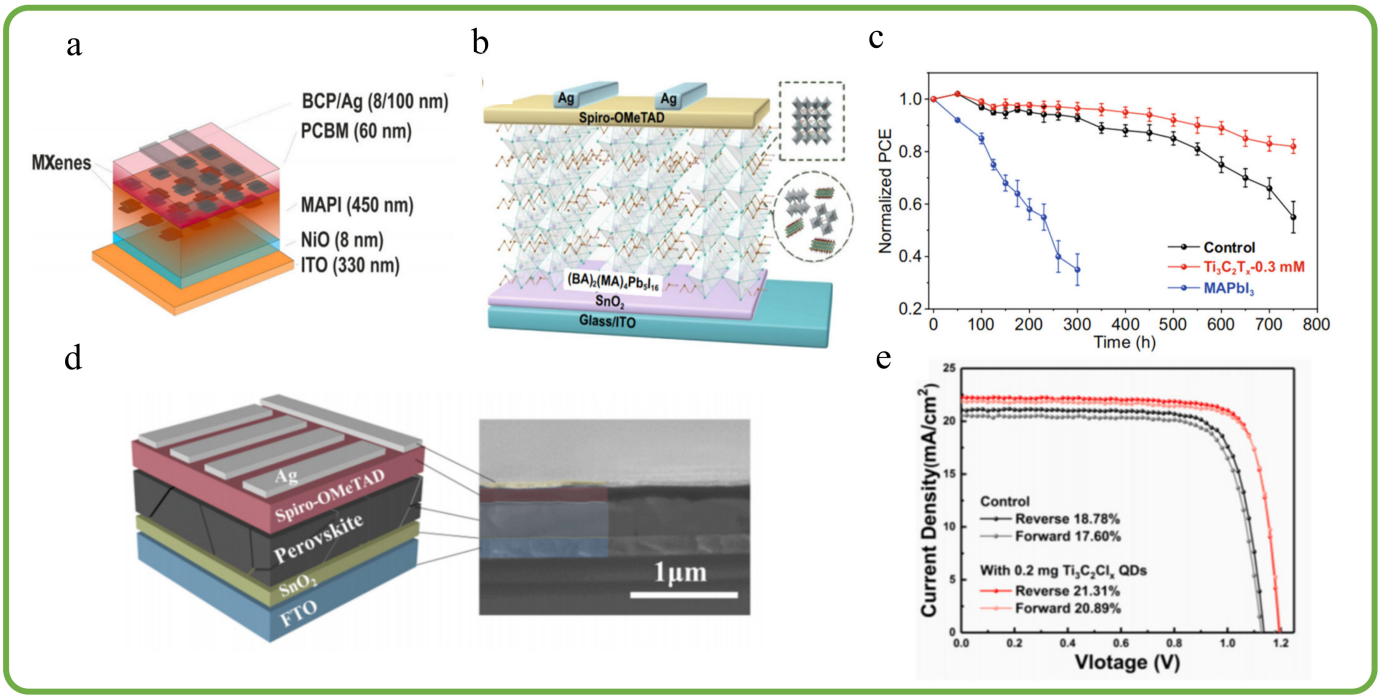

Figure 8. (**a**) Schematic representation of MXenes-based p-i-n PSCs. Reproduction with permission from ref. [114]. Copyright 2021, Elsevier; (**b**) schematic diagram of devices with the structure of Glass/ITO/SnO_2/2D perovskite/Spiro-OMeTAD/Ag. (**c**) Stability of $MAPbI_3$-based, control, and $Ti_3C_2T_x$-doping devices without sealing at air atmosphere with humidity of 55 ± 5%. Reproduction with permission from ref. [120]. Copyright 2021, Springer Nature; (**d**) schematic illustration of the device structure with colored cross-sectional SEM; (**e**) reverse and forward scans for the pristine and 0.2 mg/mL $Ti_3C_2Cl_x$ QD-treated devices. Reproduction with permission from ref. [121]. Copyright 2021, Elsevier.

In n-i-p planar PSCs, the high crystallinity of the perovskite film and its long-term stability under high humidity are crucial for achieving optimal photovoltaic performance and facilitating future commercialization. Chen et al. investigated the use of chlorine-terminated MXene quantum dots ($Ti_3C_2Cl_x$ QDs) as additives in PSCs (Figure 8d,e). They introduced $Ti_3C_2Cl_x$ QDs into the perovskite precursor solution through a one-step deposition method [121]. The strong interaction between $Ti_3C_2Cl_x$ quantum dots (QDs) and Pb^{2+} ions can reduce the crystallization rate of perovskite and promote preferred grain orientation. This interaction results in the formation of high-quality perovskite films characterized by enhanced crystallinity, fewer trap states, and reduced residual tensile strain. Additionally, the gradient distribution of $Ti_3C_2Cl_x$ QDs accelerates charge extraction and optimizes the energy band alignment between the perovskite layer and the SnO_2 electron transport layer. Ultimately, devices incorporating $Ti_3C_2Cl_x$ QDs have achieved a remarkable efficiency of 21.31%, with an open circuit voltage of 1.19 V and minimal hysteresis. Furthermore, the incorporation of $Ti_3C_2Cl_x$ QDs prevents the deprotonation of organic amines, which may occur due to OH-terminated $Ti_3C_2Cl_x$, thereby enhancing overall stability. Unencapsulated devices retain over 84% of their initial PCE after 1000 h of dark storage at 40% relative humidity, demonstrating excellent long-term humidity stability [121].

Planar PSCs fabricated using a two-step deposition method offer notable advantages in PCE. However, achieving complete conversion of compact PbI_2 to the perovskite $MAPbI_3$ poses significant challenges. To tackle this challenge, Qi et al. pioneered the introduction of $Ti_3C_2Cl_x$ MXenes nanosheets into the PbI_2 layer as multifunctional additives, thereby enhancing the reactivity of PbI_2 and facilitating the formation of porous channels [122]. Enhancements to this structure promote the reaction with CH_3NH_3I (MAI), leading to the complete conversion of PbI_2, a significant reduction of residual PbI_2 in the perovskite film,

and an increase in the size of perovskite grains. Furthermore, $Ti_3C_2Cl_x$ regulates the work function of the perovskite, optimizing the energy level alignment and facilitating the extraction and injection of charge carriers. Results indicate that functional groups on the $Ti_3C_2Cl_x$ surface passivate defects by interacting with non-coordinated Pb^{2+} in the perovskite, which significantly reduces hysteresis and suppresses non-radiative recombination. Ultimately, the researchers attained a maximum PCE of 19.27% by adding 0.03 wt% $Ti_3C_2Cl_x$. For example, Satish Bykkam and colleagues incorporated MXenes representing an approximate 18% increase over the control group. Furthermore, numerous researchers have explored the use of MXenes as additives in the perovsk with varying volume percentages ranging from 0% to 20% into the perovskite ($MAPbI_3$) [123]. The experiment demonstrated that adding 5% by volume of MXenes significantly enhances the PCE of PSCs, raising it from 11.35% to 13.62%. As the volume percentage of MXenes increases, the crystalline structure and morphology of the perovskite are modified, especially at the 5% addition level, where defect states in the perovskite film are significantly reduced, resulting in enhanced photoresponse capability. However, when the concentration of MXenes exceeds 5%, the surplus MXenes cause stacking of their lamellar structure within the perovskite light-absorbing layer. This stacking hinders light propagation and reduces the generation of photogenerated carriers, leading to a gradual decrease in J_{SC} and a decline in PCE. Li et al. incorporated two types of MXene materials—$Ti_3C_2T_x$ and vanadium carbide (V_2CT_x)—in appropriate mass fractions into the lead iodide (PbI_2) precursor solution and prepared perovskite films using a one-step coating method [124]. The optimal concentration of the V_2CT_x additive is 0.0013 wt%, achieving a PCE of 17.61%, which is an improvement of 17% compared to the control device without the additive. Regarding stability, the device containing the V_2CT_x additive maintained 68.29% of its initial PCE after 15 days, exceeding the performance of both the device without the additive and the device with $Ti_3C_2T_x$. The high electronic conductivity and carrier mobility of MXene nanosheets render them effective additives for PSCs. A.S.R. Bati and colleagues functionalized the surface of MXene by introducing cesium ions, which enhanced the interaction between MXene and perovskite films, leading to significant improvements in photovoltaic efficiency and thermal stability [125]. The incorporation of Cs-$Ti_3C_2T_x$ MXene slowed the nucleation process of perovskite, facilitating the formation of larger grains, which reduced grain boundaries, lowered defect density, and minimized non-radiative recombination. These enhancements enabled the efficiency of PSCs to surpass 21%, while also demonstrating excellent thermal stability.

3.3. MXenes as Electrodes or Additives in Electrodes

The high cost of traditional hole transport materials (HTMs) and precious metal electrodes hinders the broad application of PSCs. In response to this challenge, researchers are investigating carbon materials as alternatives to HTMs and non-precious metal PSCs. Nevertheless, while carbon materials perform well in some respects, Ti_3C_2 shows greater potential because of its superior conductivity and enhanced interface contact characteristics. Cao et al. were pioneers in utilizing Ti_3C_2 as the back electrode for HTMs and non-precious metal PSCs, creating a seamless interface contact between the perovskite layer and Ti_3C_2 using a straightforward hot-pressing method [126]. Researchers obtained Ti_3C_2 materials by etching Ti_3AlC_2 powder with hydrofluoric acid (HF) and characterized the materials using techniques such as XRD and X-ray photoelectron spectroscopy (XPS), confirming the successful synthesis of Ti_3C_2. After optimizing key parameters, PSCs based on Ti_3C_2 electrodes exhibited a higher PCE of 13.83%, which represents a 27% increase compared to PSCs based on carbon electrodes (10.87%) [126]. Furthermore, this study investigated how the thickness of the Ti_3C_2 electrode affects photovoltaic performance. Results indicated that increased electrode thickness leads to a decrease in sheet resistance, which subsequently enhances the open-circuit voltage, short-circuit current, and fill factor. The preparation process diagram of the Ti_3C_2 electrode, J-V curve, and IPCE curve are shown in Figure 9a–c.

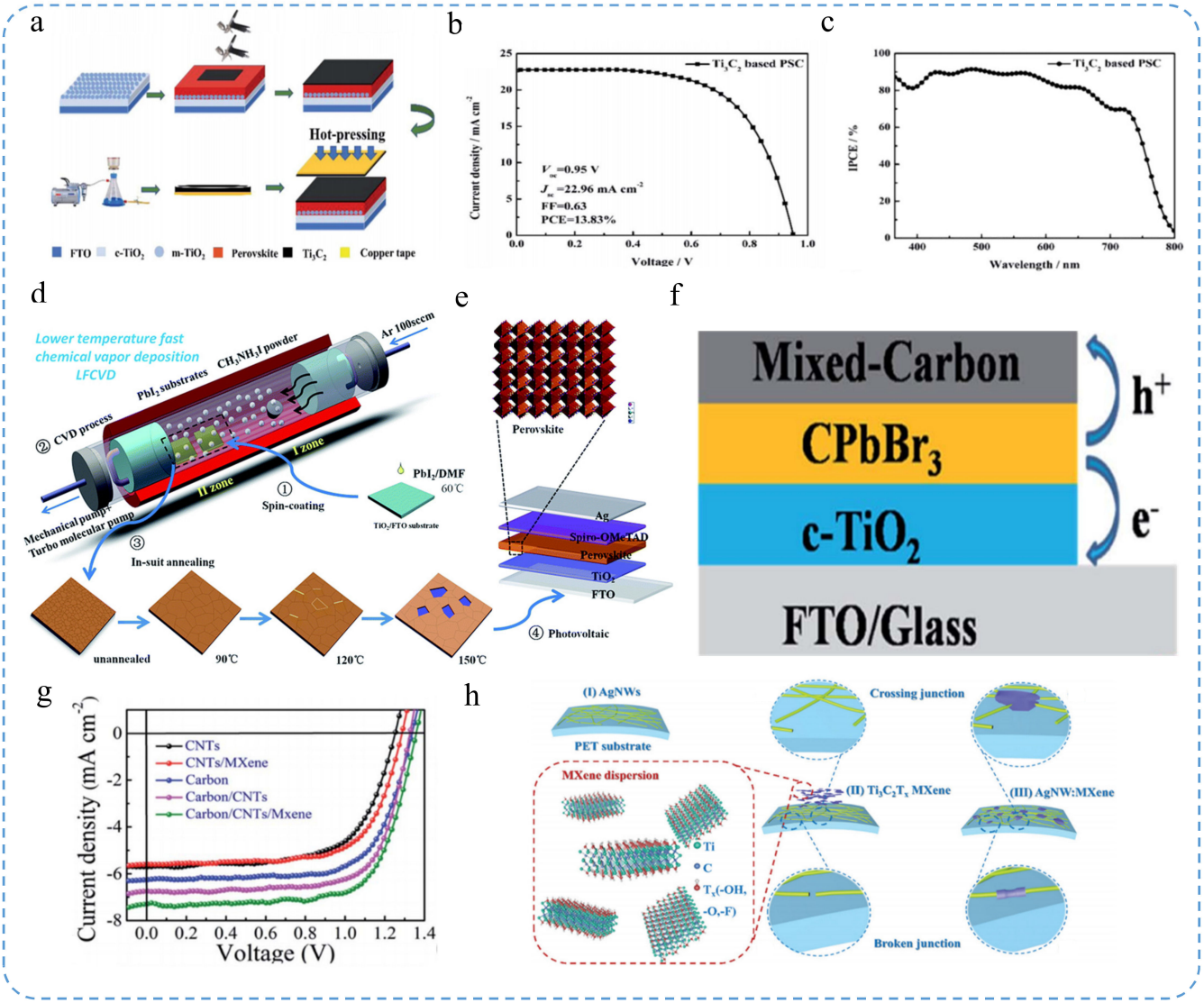

Figure 9. (**a**) Schematic diagram of the fabrication process of Ti_3C_2 electrode by hot-pressing method; (**b**) J-V curves of the champion device based on the Ti_3C_2 electrode; (**c**) IPCE of the champion device. Reproduction with permission from ref. [126]. Copyright 2019, The Royal Society of Chemistry; (**d**) schematic diagram of the configuration of the two-temperature-zones furnace tube and the fabrication procedure of a lower temperature fast chemical vapor deposition process (LFCVD) for synthesizing perovskite ($CH_3NH_3PbI_3$) films; (**e**) the multilayer structure of the final perovskite photovoltaic detector. Reproduction with permission from ref. [127]. Copyright 2017, The Royal Society of Chemistry; (**f**) schematic structure of the mixed carbon electrode $CsPbBr_3$ solar cell. (**g**) J-V curves of the devices with different types of electrodes. Reproduction with permission from ref. [128]. Copyright 2020, The Royal Society of Chemistry; (**h**) schematic of the $Ti_3C_2T_x$ MXenes and the fabrication procedure of AgNW:MXenes flexible transparent conductive electrodes. Reproduction with permission from ref. [129]. Copyright 2022, The Royal Society of Chemistry.

Traditional methods for fabricating perovskite thin films, including solution techniques and thermal evaporation, frequently encounter difficulties in reaction control during large-scale production. This variability can result in inconsistent film quality, adversely affecting device performance. Consequently, researchers are exploring cost-effective, scalable, and reliable fabrication techniques to develop high-performance perovskite optoelectronic devices. As shown in Figure 9d,e, Tong et al. introduced a rapid chemical vapor deposition (LFCVD) method performed at temperatures below 120 °C, which can produce

high-quality perovskite films in just 20 min [127]. The researchers developed perovskite photodetectors that demonstrate remarkably fast response times, with rise and fall durations of 460 ns and 940 ns, respectively. Additionally, these devices achieved a 3 dB bandwidth exceeding 0.9 MHz without the need for an external power supply. At that time, these performance metrics were unparalleled among large-area detectors (greater than 0.1 cm^2). Regarding stability, the fabricated perovskite photodetectors sustained effective performance even after exposure to ambient air for more than two months, without the necessity for special packaging.

Traditional carbon electrodes exhibit a high density of micropores formed from contact points between particles, which leads to inefficient carrier transport. In contrast, hybrid electrode designs enhance conductivity by establishing a three-dimensional pathway for carrier transport. Mi et al. implemented a hybrid carbon electrode design incorporating one-dimensional CNTs and 2D Ti_3C_2-MXene nanosheets within commercial carbon paste, as shown in Figure 9f,g. This approach facilitated the fabrication of $CsPbBr_3$-based solar cells structured as FTO/c-TiO_2/$CsPbBr_3$/hybrid carbon electrodes [128]. The results show that the introduction of CNTs provides high conductivity and rapid carrier transport channels, allowing the hybrid carbon electrode solar cells to achieve a PCE (PCE) of 7.09%, which represents a significant improvement over the performance of pure carbon electrodes. Moreover, the hybrid carbon electrodes exhibit good stability in humid environments, maintaining 80% of their initial performance after one month of air storage [128].

To address the inherent limitations of traditional indium tin oxide (ITO) electrodes in flexible devices, primarily due to their brittleness and high production costs, Chen et al. explored the potential of composite materials composed of $Ti_3C_2T_x$ and silver nanowires (AgNWs) as superior alternatives to ITO, as shown in Figure 9h [129]. The researchers successfully integrated one-dimensional AgNWs with $Ti_3C_2T_x$ nanosheets via electrostatic interactions, forming a composite electrode characterized with a distinctive 1D:2D architecture. The MXenes nanosheets effectively filled the gaps within the AgNW network and fused the junctions between the wires through capillary forces, thereby significantly improving the conductivity of the electrode. The optimized AgNW:MXenes flexible transparent electrodes (FTEs) demonstrated a resistance as low as 10.91 Ω/sq and a transmittance of up to 82.84%, indicating exceptional optoelectronic performance. Furthermore, the AgNW:MXenes FTEs exhibited high mechanical stability after undergoing 1000 bending tests and demonstrated good long-term stability under conditions of 60% relative humidity and 120 °C. The flexible PSCs and organic photovoltaics (OPVs) fabricated using this electrode achieved PCE of 20.22% and 16.03%, respectively, while retaining over 90% of their initial efficiencies during bending tests [129].

Additionally, Zhang et al. focused on $Ti_3C_2T_x$ MXenes in an attempt to replace traditional transparent conductive electrode materials, indium tin oxide (ITO) [130]. $Ti_3C_2T_x$ MXenes electrodes demonstrate remarkable conductivity in flexible organic solar cells (OSCs), achieving values as high as 6500 S/cm. This high conductivity not only enhances the PCE of the cells but also improves their mechanical stability. Liang et al. successfully synthesized transparent, conductive, and flexible MXenes/AgNW composite films through a straightforward aqueous processing method, achieving a performance index of 162.49, the highest reported in the literature [131]. The hybrid membrane demonstrates excellent conductivity, high optical transparency, low roughness, and robust mechanical properties, rendering it suitable for flexible electronic devices. In this study, hybrid electrodes were utilized in the fabrication of organic photovoltaic devices incorporating a ternary structure of PBDB-T:ITIC:$PC_{71}BM$, achieving a PCE of 8.30%. Furthermore, after conducting 1000 bending tests, the device retained 84.6% of its initial PCE, indicating excellent mechanical stability. This research not only highlights the potential of MXenes as transparent conductive electrodes but also offers new insights for future flexible optoelectronic devices, thereby advancing the development of 2D materials in optoelectronic applications.

As shown in Table 2, this article summarizes the application of MXene materials in PSCs. This includes the use of MXene materials as additives in the perovskite layer, as well as their direct use as electrodes or as additives within the electrodes.

Table 2. The role of MXenes as additives in PSC perovskite absorption layers or MXenes as additives in electrodes or electrodes.

Device Structure	J_{SC} (mA/cm^2)	V_{OC} (V)	FF (%)	PCE (%)	Refs
ITO/SnO_2/Perovskite: $Ti_3C_2T_x$/Spiro-MeOTAD/Au	22.26	1.030	76.00	17.41	[58]
TO/T-Nb_2CT_x/$FA_{0.85}Cs_{0.15}PbI_3$ + T-Nb_2CT_x/Spiro-OMeTAD/Ag	25.07	1.124	77.36	21.79	[93]
With PFN-P1 (PEDOT:PSS/PFN-P1/Perovskite/PCBM/PFN-P2/Ag)	18.75	0.930	75.00	13.20	[118]
OMXene-6 h 10 wt% (Reverse Scan)	19.86	1.210	81.96	19.69	[119]
FTO/SnO_2/$Rb_{0.05}Cs_{0.05}(FA_{0.83}MA_{0.17})_{0.90}Pb(I_{0.83}Br_{0.17})_3$:$Ti_3C_2T_x$ QDs/Spiro-OMeTAD/Au	22.27	1.190	80.42	21.31	[121]
ITO/SnO_2/$FA_{1-x}MA_xPbI_{3-y}Bry$:Cs-$Ti_3C_2T_x$/Spiro-OMeTAD/Au	26.00	1.100	76.00	21.57	[125]
FTO/C&M TiO_2/perovskite/Ti_3C_2	22.97	0.950	63.00	13.83	[126]
FTO/c-TiO_2/$CH_3NH_3PbI_3$/Spiro-OMeTAD/Ag	21.25	1.030	69.00	15.10	[127]
$CsPbBr_3$ with mixed carbon/CNT/MXene	7.16	1.360	72.97	7.09	[128]
PET/AgNW:MXene/NiO_x/perovskite/$PC_{61}BM$/Ag	25.16	1.060	75.52	20.22	[129]
PET/AgNW:MXene/PEDOT:PSS/PM6:BTP-eC9/PDINO/Al	25.65	0.850	73.61	16.03	

4. Prospects and Conclusions

This review provides a comprehensive analysis of the synthesis processes of MXenes and their multifaceted applications in PSCs. MXenes, which constitute a class of 2D transition metal carbides, nitrides, and carbonitrides, have emerged as promising materials in the field of PSCs. Their exceptional physical and chemical properties, including high conductivity, carrier mobility, optical transparency, and chemical stability, position MXenes as ideal candidates for various components within PSC architectures. Due to their remarkable physical and chemical properties, such as high electrical conductivity, carrier mobility, optical transparency, and chemical stability, MXenes are considered ideal candidates for various components in PSC architectures. However, their complex preparation processes, high costs, and potential for introducing defects or affecting interface performance limit their widespread adoption in large-scale production and practical applications. Furthermore, the environmental stability of MXenes and their interface compatibility with other materials still require further optimization to fully unleash their potential in perovskite solar cells. By classifying MXenes according to their functions as interface layers—namely, electron transport layers, perovskite absorption layers, and electrodes or additives—we have elucidated their specific contributions to enhancing PSC performance. The unique advantages of MXenes in each of these roles have been comprehensively analyzed, underscoring their potential as multifaceted materials in PSC technology.

Despite the considerable progress achieved in integrating MXenes into PSCs, several challenges persist that must be addressed to fully exploit their potential. Firstly, the scalability of MXenes' synthesis requires enhancement to satisfy the demands of large-scale production for commercial applications. Although current synthesis methods are effective in laboratory environments, they frequently lack the scalability necessary for industrial-scale manufacturing. Secondly, further research is essential to comprehend the long-term stability of MXenes within PSC devices. Preliminary investigations have yielded promising outcomes; however, to effectively address degradation pathways, it is imperative to conduct long-term stability tests under diverse environmental conditions to ensure the reliability of PSC devices. Moreover, the incorporation of MXenes with other advanced materials and technologies warrants exploration to further augment PSC performance. For example, integrating MXenes with perovskite materials that demonstrate enhanced stability and reduced toxicity could facilitate the development of more sustainable and efficient PSC devices. Additionally, the integration of MXenes in tandem solar cells—wherein multiple absorber layers are stacked to capture a broader spectrum of sunlight—holds the potential to enhance PCEs and overall system performance. Future research should prioritize the development of innovative methodologies for the precise control and modulation

of MXenes' surface chemistry and properties. Such advancements could facilitate the design of MXenes with tailored electronic and optical characteristics, optimized for specific applications in PSC devices. Finally, it is imperative to evaluate the economic feasibility of incorporating MXenes into PSC technology. While MXenes present potential cost savings as transparent electrodes, a comprehensive cost–benefit analysis must encompass the entire supply chain, including synthesis, processing, and integration into PSC devices.

In summary, MXenes have shown considerable promise in enhancing the performance of PSCs due to their versatile applications and unique properties. As research advances, MXenes are anticipated to play an increasingly pivotal role in the development of next-generation photovoltaic technologies. Future research should prioritize the optimization of MXene-based device architectures to enhance material stability and investigate novel synthesis pathways. Additionally, emphasis should be placed on exploring the application of MXene materials in PSCs to improve their performance, with particular attention to stability and PCE. Furthermore, it is essential to examine the trajectory of large-scale commercialization, seeking balance between economic viability and environmental sustainability. The outlook for PSC research incorporating MXenes is promising, with the potential to drive significant advancements in the field of photovoltaics and contribute to a sustainable energy future.

Author Contributions: B.L. and X.W. collated documents and wrote the manuscript; C.W. and X.S. (Xiaohao Shi) collaborated with the selection, preparation, and revision of the manuscript; K.T. and S.W. polished the language; X.S. (Xiangqian Shen) and Z.Y. collaborated in the revision of the manuscript. All authors have read and agreed to the published version of the manuscript.

Funding: This project was supported by the Natural Science Foundation of Xinjiang Uygur Autonomous Region of China (Grant No. 2022D01C20), the Tianshan Innovation Team Program of Xinjiang Uygur Autonomous Region of China (2023D14001).

Institutional Review Board Statement: Not applicable.

Informed Consent Statement: Not applicable.

Data Availability Statement: Data are contained within the article.

Conflicts of Interest: All authors declare that the research was conducted in the absence of any commercial or financial relationships that could be construed as a potential conflict of interest.

References

1. Kojima, A.; Teshima, K.; Shirai, Y.; Miyasaka, T. Organometal Halide Perovskites as Visible-Light Sensitizers for Photovoltaic Cells. *J. Am. Chem. Soc.* **2009**, *131*, 6050–6051. [CrossRef] [PubMed]
2. Jena, A.K.; Kulkarni, A.; Miyasaka, T. Halide Perovskite Photovoltaics: Background, Status, and Future Prospects. *Chem. Rev.* **2019**, *119*, 3036–3103. [CrossRef] [PubMed]
3. Zhou, J.; Tan, L.; Liu, Y.; Li, H.; Liu, X.; Li, M.; Wang, S.; Zhang, Y.; Jiang, C.; Hua, R.; et al. Highly efficient and stable perovskite solar cells via a multifunctional hole transporting material. *Joule* **2024**, *8*, 1691–1706. [CrossRef]
4. Nazir, G.; Lee, S.Y.; Lee, J.H.; Rehman, A.; Lee, J.K.; Seok, S.I.; Park, S.J. Stabilization of Perovskite Solar Cells: Recent Developments and Future Perspectives. *Adv. Mater.* **2022**, *34*, e2204380. [CrossRef] [PubMed]
5. Sha, W.E.I.; Ren, X.; Chen, L.; Choy, W.C.H. The efficiency limit of CH3NH3PbI3 perovskite solar cells. *Appl. Phys. Lett.* **2015**, *106*, 221104. [CrossRef]
6. Saliba, M.; Matsui, T.; Seo, J.Y.; Domanski, K.; Correa-Baena, J.P.; Nazeeruddin, M.K.; Zakeeruddin, S.M.; Tress, W.; Abate, A.; Hagfeldt, A.; et al. Cesium-containing triple cation perovskite solar cells: Improved stability, reproducibility and high efficiency. *Energy Environ. Sci.* **2016**, *9*, 1989–1997. [CrossRef]
7. Roy, P.; Kumar Sinha, N.; Tiwari, S.; Khare, A. A review on perovskite solar cells: Evolution of architecture, fabrication techniques, commercialization issues and status. *Sol. Energy* **2020**, *198*, 665–688. [CrossRef]
8. Chen, J.; Park, N.G. Causes and Solutions of Recombination in Perovskite Solar Cells. *Adv. Mater.* **2019**, *31*, e1803019. [CrossRef]
9. Lim, K.G.; Ji, S.G.; Kim, J.Y.; Lee, T.W. Effect of Interfacial Layers on the Device Lifetime of Perovskite Solar Cells. *Small Methods* **2020**, *4*, 2000065. [CrossRef]
10. Zhang, C.; Wang, Y.; Lin, X.; Wu, T.; Han, Q.; Zhang, Y.; Han, L. Effects of A site doping on the crystallization of perovskite films. *J. Mater. Chem. A* **2021**, *9*, 1372–1394. [CrossRef]
11. Kim, J.Y.; Lee, J.W.; Jung, H.S.; Shin, H.; Park, N.G. High-Efficiency Perovskite Solar Cells. *Chem. Rev.* **2020**, *120*, 7867–7918. [CrossRef] [PubMed]

12. Saki, Z.; Byranvand, M.M.; Taghavinia, N.; Kedia, M.; Saliba, M. Solution-processed perovskite thin-films: The journey from lab- to large-scale solar cells. *Energy Environ. Sci.* **2021**, *14*, 5690–5722. [CrossRef]
13. Costa, J.C.S.; Azevedo, J.; Araújo, J.P.; Santos, L.M.N.B.F.; Mendes, A. High purity and crystalline thin films of methylammonium lead iodide perovskites by a vapor deposition approach. *Thin Solid. Film.* **2018**, *664*, 12–18. [CrossRef]
14. Wang, K.; Yang, D.; Wu, C.; Sanghadasa, M.; Priya, S. Recent progress in fundamental understanding of halide perovskite semiconductors. *Prog. Mater. Sci.* **2019**, *106*, 100580. [CrossRef]
15. Fu, H. Review of lead-free halide perovskites as light-absorbers for photovoltaic applications: From materials to solar cells. *Sol. Energy Mater. Sol. Cells* **2019**, *193*, 107–132. [CrossRef]
16. Mora-Seró, I. How Do Perovskite Solar Cells Work? *Joule* **2018**, *2*, 585–587. [CrossRef]
17. Shen, X.; Lin, X.; Peng, Y.; Zhang, Y.; Long, F.; Han, Q.; Wang, Y.; Han, L. Two-Dimensional Materials for Highly Efficient and Stable Perovskite Solar Cells. *Nanomicro Lett.* **2024**, *16*, 201. [CrossRef]
18. Wang, P.; Wu, Y.; Cai, B.; Ma, Q.; Zheng, X.; Zhang, W.H. Solution-Processable Perovskite Solar Cells toward Commercialization: Progress and Challenges. *Adv. Funct. Mater.* **2019**, *29*, 1807661. [CrossRef]
19. Nie, W.; Tsai, H.; Asadpour, R.; Blancon, J.-C.; Neukirch, A.J.; Gupta, G.; Crochet, J.J.; Chhowalla, M.; Tretiak, S.; Alam, M.A.; et al. High-efficiency solution-processed perovskite solar cells with millimeter-scale grains. *Science* **2014**, *347*, 522–525. [CrossRef]
20. Correa-Baena, J.-P.; Saliba, M.; Buonassisi, T.; Grätzel, M.; Abate, A.; Hagfeldt, A. Promises and challenges of perovskite solar cells. *Scince* **2017**, *358*, 739–744. [CrossRef]
21. Lee, J.-W.; Bae, S.-H.; De Marco, N.; Hsieh, Y.-T.; Dai, Z.; Yang, Y. The role of grain boundaries in perovskite solar cells. *Mater. Today Energy* **2018**, *7*, 149–160. [CrossRef]
22. Chen, B.; Rudd, P.N.; Yang, S.; Yuan, Y.; Huang, J. Imperfections and their passivation in halide perovskite solar cells. *Chem. Soc. Rev.* **2019**, *48*, 3842–3867. [CrossRef] [PubMed]
23. Boyd, C.C.; Cheacharoen, R.; Leijtens, T.; McGehee, M.D. Understanding Degradation Mechanisms and Improving Stability of Perovskite Photovoltaics. *Chem. Rev.* **2019**, *119*, 3418–3451. [CrossRef] [PubMed]
24. Jeong, J.; Kim, M.; Seo, J.; Lu, H.; Ahlawat, P.; Mishra, A.; Yang, Y.; Hope, M.A.; Eickemeyer, F.T.; Kim, M.; et al. Pseudo-halide anion engineering for alpha-$FAPbI_3$ perovskite solar cells. *Nature* **2021**, *592*, 381–385. [CrossRef]
25. Zhang, Z.; Li, Z.; Meng, L.; Lien, S.Y.; Gao, P. Perovskite-Based Tandem Solar Cells: Get the Most Out of the Sun. *Adv. Funct. Mater.* **2020**, *30*, 2001904. [CrossRef]
26. Palei, S.; Murali, G.; Kim, C.H.; In, I.; Lee, S.Y.; Park, S.J. A Review on Interface Engineering of MXenes for Perovskite Solar Cells. *Nanomicro Lett.* **2023**, *15*, 123. [CrossRef]
27. Ren, X.; Wang, J.; Lin, Y.; Wang, Y.; Xie, H.; Huang, H.; Yang, B.; Yan, Y.; Gao, Y.; He, J.; et al. Mobile iodides capture for highly photolysis- and reverse-bias-stable perovskite solar cells. *Nat. Mater.* **2024**, *23*, 810–817. [CrossRef]
28. Chen, Y.; Peng, X.; Qin, W.; Li, S.; Zhang, L.; Wang, Y.; Chen, Z.; Yang, B.; Yuan, Y.; He, J.; et al. Filterless Bandpass Photodetectors Enabled by 2D/3D Perovskite Heterojunctions. *Adv. Funct. Mater.* **2024**, *34*, 2403942. [CrossRef]
29. Guo, P.; Dong, J.; Xu, C.; Yao, Y.; You, J.; Bian, H.; Zeng, W.; Zhou, G.; He, X.; Wang, M.; et al. Fabrication of an ultrathin PEG-modified PEDOT:PSS HTL for high-efficiency Sn–Pb perovskite solar cells by an eco-friendly solvent etching technique. *J. Mater. Chem. A* **2023**, *11*, 7246–7255. [CrossRef]
30. Yao, Y.; Lv, F.; Zhao, X.; Yang, X.; Wu, B.; Li, P.; Song, Q. A monolithic all-perovskite tandem solar cell with 2-T, 3-T and 4-T architecture integrated. *Sol. Energy Mater. Sol. Cells* **2023**, *259*, 112376. [CrossRef]
31. Wang, J.; Pan, Y.; Zhou, Z.; Zhou, Q.; Liu, S.; Zhang, J.; Shi, C.; Chen, R.; Zhao, Z.; Cai, Z.; et al. Bimolecular Crystallization Modulation Boosts the Efficiency and Stability of Methylammonium-Free Tin–Lead Perovskite and All-Perovskite Tandem Solar Cells. *Adv. Energy Mater.* **2024**, *14*, 2402171. [CrossRef]
32. Dhamodharan, D.; Dhinakaran, V.; Byun, H.-S. MXenes: An emerging 2D material. *Carbon* **2022**, *192*, 366–383. [CrossRef]
33. Li, X.; Huang, Z.; Shuck, C.E.; Liang, G.; Gogotsi, Y.; Zhi, C. MXene chemistry, electrochemistry and energy storage applications. *Nat. Rev. Chem.* **2022**, *6*, 389–404. [CrossRef]
34. Hong, W.; Wyatt, B.C.; Nemani, S.K.; Anasori, B. Double transition-metal MXenes: Atomistic design of two-dimensional carbides and nitrides. *MRS Bull.* **2020**, *45*, 850–861. [CrossRef]
35. Khazaei, M.; Ranjbar, A.; Arai, M.; Sasaki, T.; Yunoki, S. Electronic properties and applications of MXenes: A theoretical review. *J. Mater. Chem. C* **2017**, *5*, 2488–2503. [CrossRef]
36. Yang, L.; Li, P.; Ma, J.; Zhang, X.; Wang, X.-F.; Liu, Y. MXenes for perovskite solar cells: Progress and prospects. *J. Energy Chem.* **2023**, *81*, 443–461. [CrossRef]
37. Dehingia, A.; Das, U.; Mandal, D.; Roy, A. Application of $Ti_3C_2T_x$ MXene nanosheets and quantum-dots in halide perovskite solar cells. *Mater. Today Sustain.* **2024**, *25*, 100619. [CrossRef]
38. Marimuthu, S.; Prabhakaran Shyma, A.; Sathyanarayanan, S.; Gopal, T.; James, J.T.; Nagalingam, S.P.; Gunaseelan, B.; Babu, S.; Sellappan, R.; Grace, A.N. The dawn of MXene duo: Revolutionizing perovskite solar cells with MXenes through computational and experimental methods. *Nanoscale* **2024**, *16*, 10108–10141. [CrossRef]
39. Sufiyan, K.M.; Prabakaran, K. A review of the revolutionary impact of MXene marvel in perovskite solar cells. *Chem. Phys. Impact* **2024**, *8*, 100610. [CrossRef]

40. Aftab, S.; Abbas, A.; Iqbal, M.Z.; Hussain, S.; Kabir, F.; Hegazy, H.H.; Xu, F.; Kim, J.H.; Goud, B.S. Two-dimensional MXene incorporating for electron and hole transport in high-performance perovskite solar cells. *Mater. Today Energy* **2023**, *36*, 101366. [CrossRef]
41. Singh, M.; Singh, A.K. Performance improvement of photovoltaic: Utilization of two-dimensional Ti_3C_2Tx MXene. *Surf. Interfaces* **2021**, *27*, 101566. [CrossRef]
42. Shi, Z.; Khaledialidusti, R.; Malaki, M.; Zhang, H. MXene-Based Materials for Solar Cell Applications. *Nanomaterials* **2021**, *11*, 3170. [CrossRef] [PubMed]
43. Kim, H.; Wang, Z.; Alshareef, H.N. MXetronics: Electronic and photonic applications of MXenes. *Nano Energy* **2019**, *60*, 179–197. [CrossRef]
44. Wu, Y.; Sun, Y.; Zheng, J.; Rong, J.; Li, H.; Niu, L. Exploring MXene-based materials for next-generation rechargeable batteries. *J. Phys. Energy* **2021**, *3*, 032009. [CrossRef]
45. Qamar, S.; Fatima, K.; Ullah, N.; Akhter, Z.; Waseem, A.; Sultan, M. Recent progress in use of MXene in perovskite solar cells: For interfacial modification, work-function tuning and additive engineering. *Nanoscale* **2022**, *14*, 13018–13039. [CrossRef]
46. Fan, X.; Ding, Y.; Liu, Y.; Liang, J.; Chen, Y. Plasmonic Ti3C2Tx MXene Enables Highly Efficient Photothermal Conversion for Healable and Transparent Wearable Device. *ACS Nano* **2019**, *13*, 8124–8134. [CrossRef]
47. Sun, Y.; Jin, D.; Sun, Y.; Meng, X.; Gao, Y.; Dall'Agnese, Y.; Chen, G.; Wang, X.-F. g-C_3N_4/$Ti_3C_2T_x$ (MXenes) composite with oxidized surface groups for efficient photocatalytic hydrogen evolution. *J. Mater. Chem. A* **2018**, *6*, 9124–9131. [CrossRef]
48. Tao, Q.; Dahlqvist, M.; Lu, J.; Kota, S.; Meshkian, R.; Halim, J.; Palisaitis, J.; Hultman, L.; Barsoum, M.W.; Persson, P.O.A.; et al. Two-dimensional Mo(1.33)C MXene with divacancy ordering prepared from parent 3D laminate with in-plane chemical ordering. *Nat. Commun.* **2017**, *8*, 14949. [CrossRef]
49. Cai, Y.; Shen, J.; Ge, G.; Zhang, Y.; Jin, W.; Huang, W.; Shao, J.; Yang, J.; Dong, X. Stretchable $Ti_3C_2T_x$ MXene/Carbon Nanotube Composite Based Strain Sensor with Ultrahigh Sensitivity and Tunable Sensing Range. *ACS Nano* **2018**, *12*, 56–62. [CrossRef]
50. Lee, J.-H.; Yang, G.; Kim, C.-H.; Mahajan, R.L.; Lee, S.-Y.; Park, S.-J. Flexible solid-state hybrid supercapacitors for the internet of everything (IoE). *Energy Environ. Sci.* **2022**, *15*, 2233–2258. [CrossRef]
51. Li, Z.; Zhuang, Z.; Lv, F.; Zhu, H.; Zhou, L.; Luo, M.; Zhu, J.; Lang, Z.; Feng, S.; Chen, W.; et al. The Marriage of the FeN_4 Moiety and MXene Boosts Oxygen Reduction Catalysis: Fe 3d Electron Delocalization Matters. *Adv. Mater.* **2018**, *30*, e1803220. [CrossRef] [PubMed]
52. Ming, F.; Liang, H.; Huang, G.; Bayhan, Z.; Alshareef, H.N. MXenes for Rechargeable Batteries Beyond the Lithium-Ion. *Adv. Mater.* **2021**, *33*, e2004039. [CrossRef] [PubMed]
53. Niyitanga, T.; Chaudhary, A.; Ahmad, K.; Kim, H. Titanium Carbide ($Ti_3C_2T_x$) MXene as Efficient Electron/Hole Transport Material for Perovskite Solar Cells and Electrode Material for Electrochemical Biosensors/Non-Biosensors Applications. *Micromachines* **2023**, *14*, 1907. [CrossRef] [PubMed]
54. Dall'Agnese, Y.; Lukatskaya, M.R.; Cook, K.M.; Taberna, P.-L.; Gogotsi, Y.; Simon, P. High capacitance of surface-modified 2D titanium carbide in acidic electrolyte. *Electrochem. Commun.* **2014**, *48*, 118–122. [CrossRef]
55. Dillon, A.D.; Ghidiu, M.J.; Krick, A.L.; Griggs, J.; May, S.J.; Gogotsi, Y.; Barsoum, M.W.; Fafarman, A.T. Highly Conductive Optical Quality Solution-Processed Films of 2D Titanium Carbide. *Adv. Funct. Mater.* **2016**, *26*, 4162–4168. [CrossRef]
56. Wang, Y.; Xu, Y.; Hu, M.; Ling, H.; Zhu, X. MXenes: Focus on optical and electronic properties and corresponding applications. *Nanophotonics* **2020**, *9*, 1601–1620. [CrossRef]
57. Hantanasirisakul, K.; Gogotsi, Y. Electronic and Optical Properties of 2D Transition Metal Carbides and Nitrides (MXenes). *Adv. Mater.* **2018**, *30*, e1804779. [CrossRef]
58. Guo, Z.; Gao, L.; Xu, Z.; Teo, S.; Zhang, C.; Kamata, Y.; Hayase, S.; Ma, T. High Electrical Conductivity 2D MXene Serves as Additive of Perovskite for Efficient Solar Cells. *Small* **2018**, *14*, e1802738. [CrossRef]
59. Gogotsi, Y.; Huang, Q. MXenes: Two-Dimensional Building Blocks for Future Materials and Devices. *ACS Nano* **2021**, *15*, 5775–5780. [CrossRef]
60. Anasori, B.; Lukatskaya, M.R.; Gogotsi, Y. 2D metal carbides and nitrides (MXenes) for energy storage. *Nat. Rev. Mater.* **2017**, *2*, 16098. [CrossRef]
61. Park, S.J.; Kim, H.C.; Kim, H.Y. Roles of work of adhesion between carbon blacks and thermoplastic polymers on electrical properties of composites. *J. Colloid. Interface Sci.* **2002**, *255*, 145–149. [CrossRef] [PubMed]
62. Murali, G.; Reddy Modigunta, J.K.; Park, Y.H.; Lee, J.H.; Rawal, J.; Lee, S.Y.; In, I.; Park, S.J. A Review on MXene Synthesis, Stability, and Photocatalytic Applications. *ACS Nano* **2022**, *16*, 13370–13429. [CrossRef] [PubMed]
63. Naguib, M.; Kurtoglu, M.; Presser, V.; Lu, J.; Niu, J.; Heon, M.; Hultman, L.; Gogotsi, Y.; Barsoum, M.W. Two-Dimensional Nanocrystals Produced by Exfoliation of Ti_3AlC_2. *Adv. Mater.* **2011**, *23*, 4248–4253. [CrossRef] [PubMed]
64. VahidMohammadi, A.; Rosen, J.; Gogotsi, Y. The world of two-dimensional carbides and nitrides (MXenes). *Science* **2021**, *372*, eabf1581. [CrossRef]
65. Lim, K.R.G.; Shekhirev, M.; Wyatt, B.C.; Anasori, B.; Gogotsi, Y.; Seh, Z.W. Fundamentals of MXene synthesis. *Nat. Synth.* **2022**, *1*, 601–614. [CrossRef]
66. Deysher, G.; Shuck, C.E.; Hantanasirisakul, K.; Frey, N.C.; Foucher, A.C.; Maleski, K.; Sarycheva, A.; Shenoy, V.B.; Stach, E.A.; Anasori, B.; et al. Synthesis of Mo_4VAlC_4 MAX Phase and Two-Dimensional Mo_4VC_4 MXene with Five Atomic Layers of Transition Metals. *ACS Nano* **2020**, *14*, 204–217. [CrossRef]

67. Wei, Y.; Zhang, P.; Soomro, R.A.; Zhu, Q.; Xu, B. Advances in the Synthesis of 2D MXenes. *Adv. Mater.* **2021**, *33*, e2103148. [CrossRef]
68. Saeed, M.A.; Qamar, M.Z.; Khalid, Z.; Chamanehpour, E.; Mishra, Y.K. Two-dimensional MXenes: A route from synthesis to applications in self-powered IoT devices. *Chem. Eng. J.* **2024**, *490*, 151600. [CrossRef]
69. Alhabeb, M.; Maleski, K.; Anasori, B.; Lelyukh, P.; Clark, L.; Sin, S.; Gogotsi, Y. Guidelines for Synthesis and Processing of Two-Dimensional Titanium Carbide ($Ti_3C_2T_x$ MXene). *Chem. Mater.* **2017**, *29*, 7633–7644. [CrossRef]
70. Ronchi, R.M.; Arantes, J.T.; Santos, S.F. Synthesis, structure, properties and applications of MXenes: Current status and perspectives. *Ceram. Int.* **2019**, *45*, 18167–18188. [CrossRef]
71. Kamysbayev, V.; Filatov, A.S.; Hu, H.; Rui, X.; Lagunas, F.; Wang, D.; Klie, R.F.; Talapin, D.V. Covalent surface modifications and superconductivity of two-dimensional metal carbide MXenes. *Science* **2020**, *369*, 979–983. [CrossRef] [PubMed]
72. Shuck, C.E.; Ventura-Martinez, K.; Goad, A.; Uzun, S.; Shekhirev, M.; Gogotsi, Y. Safe Synthesis of MAX and MXene: Guidelines to Reduce Risk During Synthesis. *ACS Chem. Health Saf.* **2021**, *28*, 326–338. [CrossRef]
73. Naguib, M.; Mochalin, V.N.; Barsoum, M.W.; Gogotsi, Y. 25th anniversary article: MXenes: A new family of two-dimensional materials. *Adv. Mater.* **2014**, *26*, 992–1005. [CrossRef] [PubMed]
74. Ghidiu, M.; Lukatskaya, M.R.; Zhao, M.Q.; Gogotsi, Y.; Barsoum, M.W. Conductive two-dimensional titanium carbide 'clay' with high volumetric capacitance. *Nature* **2014**, *516*, 78–81. [CrossRef]
75. Alhabeb, M.; Maleski, K.; Mathis, T.S.; Sarycheva, A.; Hatter, C.B.; Uzun, S.; Levitt, A.; Gogotsi, Y. Selective Etching of Silicon from $Ti_3C_2T_x$ (MAX) To Obtain 2D Titanium Carbide (MXene). *Angew. Chem. Int. Ed. Engl.* **2018**, *57*, 5444–5448. [CrossRef]
76. Halim, J.; Lukatskaya, M.R.; Cook, K.M.; Lu, J.; Smith, C.R.; Näslund, L.-Å.; May, S.J.; Hultman, L.; Gogotsi, Y.; Eklund, P.; et al. Transparent Conductive Two-Dimensional Titanium Carbide Epitaxial Thin Films. *Chem. Mater.* **2014**, *26*, 2374–2381. [CrossRef]
77. Voigt, C.A.; Ghidiu, M.; Natu, V.; Barsoum, M.W. Anion Adsorption, $Ti_3C_2T_z$ MXene Multilayers, and Their Effect on Claylike Swelling. *J. Phys. Chem. C* **2018**, *122*, 23172–23179. [CrossRef]
78. Xuan, J.; Wang, Z.; Chen, Y.; Liang, D.; Cheng, L.; Yang, X.; Liu, Z.; Ma, R.; Sasaki, T.; Geng, F. Organic-Base-Driven Intercalation and Delamination for the Production of Functionalized Titanium Carbide Nanosheets with Superior Photothermal Therapeutic Performance. *Angew. Chem. Int. Ed. Engl.* **2016**, *55*, 14569–14574. [CrossRef]
79. Pang, S.Y.; Wong, Y.T.; Yuan, S.; Liu, Y.; Tsang, M.K.; Yang, Z.; Huang, H.; Wong, W.T.; Hao, J. Universal Strategy for HF-Free Facile and Rapid Synthesis of Two-dimensional MXenes as Multifunctional Energy Materials. *J. Am. Chem. Soc.* **2019**, *141*, 9610–9616. [CrossRef]
80. Ghazaly, A.E.; Ahmed, H.; Rezk, A.R.; Halim, J.; Persson, P.O.Å.; Yeo, L.Y.; Rosen, J. Ultrafast, One-Step, Salt-Solution-Based Acoustic Synthesis of Ti3C2 MXene. *ACS Nano* **2021**, *15*, 4287–4293. [CrossRef]
81. Shi, H.; Zhang, P.; Liu, Z.; Park, S.; Lohe, M.R.; Wu, Y.; Shaygan Nia, A.; Yang, S.; Feng, X. Ambient-Stable Two-Dimensional Titanium Carbide (MXene) Enabled by Iodine Etching. *Angew. Chem. Int. Ed. Engl.* **2021**, *60*, 8689–8693. [CrossRef] [PubMed]
82. Yu, X.; Cai, X.; Cui, H.; Lee, S.W.; Yu, X.F.; Liu, B. Fluorine-free preparation of titanium carbide MXene quantum dots with high near-infrared photothermal performances for cancer therapy. *Nanoscale* **2017**, *9*, 17859–17864. [CrossRef] [PubMed]
83. Wang, X.; Garnero, C.; Rochard, G.; Magne, D.; Morisset, S.; Hurand, S.; Chartier, P.; Rousseau, J.; Cabioc'h, T.; Coutanceau, C.; et al. A new etching environment (FeF_3/HCl) for the synthesis of two-dimensional titanium carbide MXenes: A route towards selective reactivity vs. water. *J. Mater. Chem. A* **2017**, *5*, 22012–22023. [CrossRef]
84. Li, M.; Lu, J.; Luo, K.; Li, Y.; Chang, K.; Chen, K.; Zhou, J.; Rosen, J.; Hultman, L.; Eklund, P.; et al. Element Replacement Approach by Reaction with Lewis Acidic Molten Salts to Synthesize Nanolaminated MAX Phases and MXenes. *J. Am. Chem. Soc.* **2019**, *141*, 4730–4737. [CrossRef]
85. Li, T.; Yao, L.; Liu, Q.; Gu, J.; Luo, R.; Li, J.; Yan, X.; Wang, W.; Liu, P.; Chen, B.; et al. Fluorine-Free Synthesis of High-Purity $Ti_3C_2T_x$ (T=OH, O) via Alkali Treatment. *Angew. Chem. Int. Ed. Engl.* **2018**, *57*, 6115–6119. [CrossRef]
86. Sun, W.; Shah, S.A.; Chen, Y.; Tan, Z.; Gao, H.; Habib, T.; Radovic, M.; Green, M.J. Electrochemical etching of Ti_2AlC to Ti_2CT_x (MXene) in low-concentration hydrochloric acid solution. *J. Mater. Chem. A* **2017**, *5*, 21663–21668. [CrossRef]
87. Yang, L.; Dall'Agnese, C.; Dall'Agnese, Y.; Chen, G.; Gao, Y.; Sanehira, Y.; Jena, A.K.; Wang, X.F.; Gogotsi, Y.; Miyasaka, T. Surface-Modified Metallic $Ti_3C_2T_x$ MXene as Electron Transport Layer for Planar Heterojunction Perovskite Solar Cells. *Adv. Funct. Mater.* **2019**, *29*, 1905694. [CrossRef]
88. Wang, J.; Cai, Z.; Lin, D.; Chen, K.; Zhao, L.; Xie, F.; Su, R.; Xie, W.; Liu, P.; Zhu, R. Plasma Oxidized Ti3C2Tx MXene as Electron Transport Layer for Efficient Perovskite Solar Cells. *ACS Appl. Mater. Interfaces* **2021**, *13*, 32495–32502. [CrossRef]
89. Chen, Z.; Lu, M.; Qian, Y.; Yang, Y.; Liu, J.; Lin, Z.; Yang, D.; Lu, J.; Qiu, X. Ultra-Low Dosage Lignin Binder for Practical Lithium–Sulfur Batteries. *Adv. Energy Mater.* **2023**, *13*, 2300092. [CrossRef]
90. Di Vito, A.; Pecchia, A.; Auf der Maur, M.; Di Carlo, A. Nonlinear Work Function Tuning of Lead-Halide Perovskites by MXenes with Mixed Terminations. *Adv. Funct. Mater.* **2020**, *30*, 1909028. [CrossRef]
91. Niu, Y.; Tian, C.; Gao, J.; Fan, F.; Zhang, Y.; Mi, Y.; Ouyang, X.; Li, L.; Li, J.; Chen, S.; et al. Nb_2C MXenes modified SnO_2 as high quality electron transfer layer for efficient and stability perovskite solar cells. *Nano Energy* **2021**, *89*, 106455. [CrossRef]
92. Yin, L.; Liu, C.; Ding, C.; Zhao, C.; Mitrovic, I.Z.; Lim, E.G.; Wang, H.; Sun, Y.; Han, Y.; Li, Z.; et al. Functionalized-MXene-nanosheet-doped tin oxide enhances the electrical properties in perovskite solar cells. *Cell Rep. Phys. Sci.* **2022**, *3*, 100905. [CrossRef]

93. Zhang, J.; Huang, C.; Sun, Y.; Yu, H. Amino-Functionalized Niobium-Carbide MXene Serving as Electron Transport Layer and Perovskite Additive for the Preparation of High-Performance and Stable Methylammonium-Free Perovskite Solar Cells. *Adv. Funct. Mater.* **2022**, *32*, 2113367. [CrossRef]
94. Wang, Z.; Zhang, D.; Yang, G.; Yu, J. Exceeding 19% efficiency for inverted perovskite solar cells used conventional organic small molecule TPD as hole transport layer. *Appl. Phys. Lett.* **2021**, *118*, 183301. [CrossRef]
95. Li, B.; Yang, K.; Liao, Q.; Wang, Y.; Su, M.; Li, Y.; Shi, Y.; Feng, X.; Huang, J.; Sun, H.; et al. Imide-Functionalized Triarylamine-Based Donor-Acceptor Polymers as Hole Transporting Layers for High-Performance Inverted Perovskite Solar Cells. *Adv. Funct. Mater.* **2021**, *31*, 2100332. [CrossRef]
96. Ma, S.; Zhang, X.; Liu, X.; Ghadari, R.; Cai, M.; Ding, Y.; Mateen, M.; Dai, S. Pyridine-triphenylamine hole transport material for inverted perovskite solar cells. *J. Energy Chem.* **2021**, *54*, 395–402. [CrossRef]
97. Mashtalir, O.; Lukatskaya, M.R.; Zhao, M.Q.; Barsoum, M.W.; Gogotsi, Y. Amine-Assisted Delamination of Nb2C MXene for Li-Ion Energy Storage Devices. *Adv. Mater.* **2015**, *27*, 3501–3506. [CrossRef]
98. Gao, L.; Ma, C.; Wei, S.; Kuklin, A.V.; Zhang, H.; Agren, H. Applications of Few-Layer Nb_2C MXene: Narrow-Band Photodetectors and Femtosecond Mode-Locked Fiber Lasers. *ACS Nano* **2021**, *15*, 954–965. [CrossRef]
99. Khazaei, M.; Arai, M.; Sasaki, T.; Ranjbar, A.; Liang, Y.; Yunoki, S. OH-terminated two-dimensional transition metal carbides and nitrides as ultralow work function materials. *Phys. Rev. B* **2015**, *92*, 075411. [CrossRef]
100. Zhang, J.; Huang, C.; Yu, H. Modulate the work function of Nb_2CT_x MXene as the hole transport layer for perovskite solar cells. *Appl. Phys. Lett.* **2021**, *119*. [CrossRef]
101. Du, J.-B.; Yang, L.; Jin, X.; Liu, C.-L.; Wang, H.-H.; Wang, X.-F. Spray deposition of vinyl tris(2-methoxyethoxy) silane-doped Ti_3C_2T MXene hole transporting layer for planar perovskite solar cells. *J. Alloys Compd.* **2022**, *900*, 163372. [CrossRef]
102. Zheng, H.; Wang, Y.; Niu, B.; Ge, R.; Lei, Y.; Yan, L.; Si, J.; Zhong, P.; Ma, X. Controlling the Defect Density of Perovskite Films by MXene/SnO_2 Hybrid Electron Transport Layers for Efficient and Stable Photovoltaics. *J. Phys. Chem. C* **2021**, *125*, 15210–15222. [CrossRef]
103. Chava, V.S.N.; Chandrasekhar, P.S.; Gomez, A.; Echegoyen, L.; Sreenivasan, S.T. MXene-Based Tailoring of Carrier Dynamics, Defect Passivation, and Interfacial Band Alignment for Efficient Planar p–i–n Perovskite Solar Cells. *ACS Appl. Energy Mater.* **2021**, *4*, 12137–12148. [CrossRef]
104. Yang, L.; Dall'Agnese, Y.; Hantanasirisakul, K.; Shuck, C.E.; Maleski, K.; Alhabeb, M.; Chen, G.; Gao, Y.; Sanehira, Y.; Jena, A.K.; et al. SnO_2–Ti_3C_2 MXene electron transport layers for perovskite solar cells. *J. Mater. Chem. A* **2019**, *7*, 5635–5642. [CrossRef]
105. Yang, Y.; Lu, H.; Feng, S.; Yang, L.; Dong, H.; Wang, J.; Tian, C.; Li, L.; Lu, H.; Jeong, J.; et al. Modulation of perovskite crystallization processes towards highly efficient and stable perovskite solar cells with MXene quantum dot-modified SnO_2. *Energy Environ. Sci.* **2021**, *14*, 3447–3454. [CrossRef]
106. Hu, W.; Liu, T.; Yin, X.; Liu, H.; Zhao, X.; Luo, S.; Guo, Y.; Yao, Z.; Wang, J.; Wang, N.; et al. Hematite electron-transporting layers for environmentally stable planar perovskite solar cells with enhanced energy conversion and lower hysteresis. *J. Mater. Chem. A* **2017**, *5*, 1434–1441. [CrossRef]
107. Guo, Y.; Liu, C.; Inoue, K.; Harano, K.; Tanaka, H.; Nakamura, E. Enhancement in the efficiency of an organic–inorganic hybrid solar cell with a doped P3HT hole-transporting layer on a void-free perovskite active layer. *J. Mater. Chem. A* **2014**, *2*, 13827–13830. [CrossRef]
108. Liu, J.; Durstock, M.; Dai, L. Graphene oxide derivatives as hole- and electron-extraction layers for high-performance polymer solar cells. *Energy Environ. Sci.* **2014**, *7*, 1297–1306. [CrossRef]
109. Lu, L.; Xu, T.; Chen, W.; Lee, J.M.; Luo, Z.; Jung, I.H.; Park, H.I.; Kim, S.O.; Yu, L. The role of N-doped multiwall carbon nanotubes in achieving highly efficient polymer bulk heterojunction solar cells. *Nano Lett.* **2013**, *13*, 2365–2369. [CrossRef]
110. Hussain, S.; Liu, H.; Vikraman, D.; Hussain, M.; Jaffery, S.H.A.; Ali, A.; Kim, H.-S.; Kang, J.; Jung, J. Characteristics of Mo_2C-CNTs hybrid blended hole transport layer in the perovskite solar cells and X-ray detectors. *J. Alloys Compd.* **2021**, *885*, 161039. [CrossRef]
111. Hussain, S.; Liu, H.; Hussain, M.; Mehran, M.T.; Kim, H.S.; Jung, J.; Vikraman, D.; Kang, J. Development ofMXene/WO_3 embedded PEDOT:PSS hole transport layers for highly efficient perovskite solar cells and X-ray detectors. *Int. J. Energy Res.* **2022**, *46*, 12485–12497. [CrossRef]
112. Akhter, R.; Maktedar, S.S. MXenes: A comprehensive review of synthesis, properties, and progress in supercapacitor applications. *J. Mater.* **2023**, *9*, 1196–1241. [CrossRef]
113. Li, Z.; Wang, P.; Ma, C.; Igbari, F.; Kang, Y.; Wang, K.L.; Song, W.; Dong, C.; Li, Y.; Yao, J.; et al. Single-Layered MXene Nanosheets Doping TiO_2 for Efficient and Stable Double Perovskite Solar Cells. *J. Am. Chem. Soc.* **2021**, *143*, 2593–2600. [CrossRef] [PubMed]
114. Saranin, D.; Pescetelli, S.; Pazniak, A.; Rossi, D.; Liedl, A.; Yakusheva, A.; Luchnikov, L.; Podgorny, D.; Gostischev, P.; Didenko, S.; et al. Transition metal carbides (MXenes) for efficient NiO-based inverted perovskite solar cells. *Nano Energy* **2021**, *82*, 105771. [CrossRef]
115. Karimipour, M.; Paingott Parambil, A.; Tabah Tanko, K.; Zhang, T.; Gao, F.; Lira-Cantu, M. Functionalized MXene/Halide Perovskite Heterojunctions for Perovskite Solar Cells Stable Under Real Outdoor Conditions. *Adv. Energy Mater.* **2023**, *13*, 2301959. [CrossRef]
116. Jung, H.S.; Park, N.G. Perovskite solar cells: From materials to devices. *Small* **2015**, *11*, 10–25. [CrossRef]

117. Listorti, A.; Juarez-Perez, E.J.; Frontera, C.; Roiati, V.; Garcia-Andrade, L.; Colella, S.; Rizzo, A.; Ortiz, P.; Mora-Sero, I. Effect of Mesostructured Layer upon Crystalline Properties and Device Performance on Perovskite Solar Cells. *J. Phys. Chem. Lett.* **2015**, *6*, 1628–1637. [CrossRef]
118. Tripathi, N.; Shirai, Y.; Yanagida, M.; Karen, A.; Miyano, K. Novel Surface Passivation Technique for Low-Temperature Solution-Processed Perovskite PV Cells. *ACS Appl. Mater. Interfaces* **2016**, *8*, 4644–4650. [CrossRef]
119. Heo, J.H.; Zhang, F.; Park, J.K.; Joon Lee, H.; Lee, D.S.; Heo, S.J.; Luther, J.M.; Berry, J.J.; Zhu, K.; Im, S.H. Surface engineering with oxidized Ti3C2Tx MXene enables efficient and stable p-i-n-structured CsPbI3 perovskite solar cells. *Joule* **2022**, *6*, 1672–1688. [CrossRef]
120. Jin, X.; Yang, L.; Wang, X.F. Efficient Two-Dimensional Perovskite Solar Cells Realized by Incorporation of $Ti_3C_2T_x$ MXene as Nano-Dopants. *Nanomicro Lett.* **2021**, *13*, 68. [CrossRef]
121. Liu, X.; Zhang, Z.; Jiang, J.; Tian, C.; Wang, X.; Wang, L.; Zhang, Z.; Wu, X.; Zheng, Y.; Liang, J.; et al. Chlorine-terminated MXene quantum dots for improving crystallinity and moisture stability in high-performance perovskite solar cells. *Chem. Eng. J.* **2022**, *432*, 134382. [CrossRef]
122. Zhao, Y.; Zhang, X.; Han, X.; Hou, C.; Wang, H.; Qi, J.; Li, Y.; Zhang, Q. Tuning the reactivity of PbI_2 film via monolayer $Ti_3C_2T_x$ MXene for two-step-processed $CH_3NH_3PbI_3$ solar cells. *Chem. Eng. J.* **2021**, *417*, 127912. [CrossRef]
123. Bykkam, S.; Mishra, A.; Prasad, D.N.; Maurya, M.R.; Cabibihan, J.-J.; Ahmad, Z.; Sadasivuni, K.K. 2D-MXene as an additive to improve the power conversion efficiency of monolithic perovskite solar cells. *Mater. Lett.* **2022**, *309*, 131353. [CrossRef]
124. Li, Y.; Wang, D.; Yang, L.; Yin, S. Preparation and performance of perovskite solar cells with two dimensional MXene as active layer additive. *J. Alloys Compd.* **2022**, *904*, 163742. [CrossRef]
125. Bati, A.S.R.; Sutanto, A.A.; Hao, M.; Batmunkh, M.; Yamauchi, Y.; Wang, L.; Wang, Y.; Nazeeruddin, M.K.; Shapter, J.G. Cesium-doped $Ti_3C_2T_x$ MXene for efficient and thermally stable perovskite solar cells. *Cell Rep. Phys. Sci.* **2021**, *2*, 100598. [CrossRef]
126. Cao, J.; Meng, F.; Gao, L.; Yang, S.; Yan, Y.; Wang, N.; Liu, A.; Li, Y.; Ma, T. Alternative electrodes for HTMs and noble-metal-free perovskite solar cells: 2D MXenes electrodes. *RSC Adv.* **2019**, *9*, 34152–34157. [CrossRef]
127. Tong, G.; Geng, X.; Yu, Y.; Yu, L.; Xu, J.; Jiang, Y.; Sheng, Y.; Shi, Y.; Chen, K. Rapid, stable and self-powered perovskite detectors via a fast chemical vapor deposition process. *RSC Adv.* **2017**, *7*, 18224–18230. [CrossRef]
128. Mi, L.; Zhang, Y.; Chen, T.; Xu, E.; Jiang, Y. Carbon electrode engineering for high efficiency all-inorganic perovskite solar cells. *RSC Adv.* **2020**, *10*, 12298–12303. [CrossRef]
129. Chen, W.; Zhang, R.; Yang, X.; Wang, H.; Yang, H.; Hu, X.; Zhang, S. A 1D:2D structured AgNW:MXene composite transparent electrode with high mechanical robustness for flexible photovoltaics. *J. Mater. Chem. C* **2022**, *10*, 8625–8633. [CrossRef]
130. Zhang, C.J.; McKeon, L.; Kremer, M.P.; Park, S.H.; Ronan, O.; Seral-Ascaso, A.; Barwich, S.; Coileain, C.O.; McEvoy, N.; Nerl, H.C.; et al. Additive-free MXene inks and direct printing of micro-supercapacitors. *Nat. Commun.* **2019**, *10*, 1795. [CrossRef]
131. Tang, H.; Feng, H.; Wang, H.; Wan, X.; Liang, J.; Chen, Y. Highly Conducting MXene-Silver Nanowire Transparent Electrodes for Flexible Organic Solar Cells. *ACS Appl. Mater. Interfaces* **2019**, *11*, 25330–25337. [CrossRef] [PubMed]